Universidade do Minho
Escola de Engenharia

Rida Jabbar

Localized spot bonding of braided composite rebars

FRP++
Advanced structural analysis and design using composite materials

Funded by the European Union

September 2026

Localized spot bonding of braided composite rebars
Rida Jabbar
FRP++ Advanced structural analysis and design using composite materials
UMinho | 2026

The European Master in Advanced Structural Analysis and Design using Composite Materials is a join initiative of:

Universidade do Minho · Universitat de Girona · Università degli Studi di Napoli Federico II · INSA Institut National des Sciences Appliquées Toulouse · Université de Toulouse

Universidade do Minho
Escola de Engenharia

Rida Jabbar

Localized spot bonding of braided composite rebars

FRP++
Advanced structural analysis and design using composite materials

Master Dissertation
European Master Advanced Structural Analysis and Design using Composite Materials

Work developed under the supervision of
Professor José Sena Cruz
Andresa Gomes

Funded by the European Union

September 2026

DIREITOS DE AUTOR E CONDIÇÕES DE UTILIZAÇÃO DO TRABALHO POR TERCEIROS

Este é um trabalho académico que pode ser utilizado por terceiros desde que respeitadas as regras e boas práticas internacionalmente aceites, no que concerne aos direitos de autor e direitos conexos.

Assim, o presente trabalho pode ser utilizado nos termos previstos na licença abaixo indicada.

Caso o utilizador necessite de permissão para poder fazer um uso do trabalho em condições não previstas no licenciamento indicado, deverá contactar o autor, através do RepositóriUM da Universidade do Minho.

Licença concedida aos utilizadores deste trabalho



Atribuição-NãoComercial-SemDerivações CC BY-NC-ND

https://creativecommons.org/licenses/by-nc-nd/4.0/

[This is the most restrictive of our six main licences, only allowing others to download your works and share them, provided that appropriate credit is given to you, but without allowing them to modify them in any way or use them for commercial purposes.]

ACKNOWLEDGEMENTS

First and foremost, I would like to express my deepest gratitude to Allah Almighty, whose blessings, guidance and strength made this entire journey possible.

I would like to sincerely thank my supervisor, Professor José Sena Cruz, for his invaluable guidance, scientific insight and continuous support throughout this dissertation. I am equally grateful to my co-supervisor, Andresa Gomes, for her constant guidance, encouragement and practical support throughout the development of this research.

I would like to gratefully acknowledge the support provided by the European Union for participation in the Erasmus Mundus FRP++ European Master Course in Advanced Structural Analysis and Design using Composite Materials (Project no. 101048961). This work was also supported by FCT/MCTES under the R&D Unit Institute for Sustainability and Innovation in Structural Engineering (ISISE), under the references UID/4029/2025 (DOI: 10.54499/UID/04029/2025), UID/PRR/04029/2025 (DOI: 10.54499/UID/PRR/04029/2025) and UID/PRR2/04029/2025 (DOI: 10.54499/UID/PRR2/04029/2025), and under the Associate Laboratory Advanced Production and Intelligent Systems ARISE under reference LA/P/0112/2020 (DOI: 10.54499/LA/P/0112/2020).

This work is also within the R&D Project "EasyWall - Development of an innovative EPS-RC multifunctional sandwich panel solution for fast, efficient and sustainable construction", project no. 18500, operation code COMPETE2030-FEDER-01491400, co-funded by the Program for the Innovation and Digital Transition (COMPETE 2030), by the Portugal 2030 and by the European Union, in its FEDER component.

I would also like to thank The Light Rebar Company (LRC) for providing the industrial context and resources for this research, and CENTI and PIEP for their collaboration and technical support.

Finally, I am deeply grateful to my parents, siblings and my partner Mohammad Awais Qamar for their unconditional love, prayers, sacrifices and constant encouragement throughout this journey.

STATEMENT OF INTEGRITY

I hereby declare having conducted this academic work with integrity. I confirm that I have not used plagiarism or any form of undue use of information or falsification of results along the process leading to its elaboration.

I further declare that I have fully acknowledged the Code of Ethics and Conduct of the University of Minho.

DECLARATION ON THE USE OF ARTIFICIAL INTELLIGENCE (AI) TOOLS

I hereby declare having acted this academic work with integrity and confirm that I have not resorted to any form of undue use of AI tools, nor to the falsification or omission of information, sources, data, results or processes in any of the stages leading to its elaboration.

I further declare that any use of AI tools was done in a transparent and responsible manner, being duly noted in the work, and that I critically verified the accuracy of the content produced with their support, assuming full responsibility for what I submit.

I further declare that I have fully acknowledged the Code of Ethics and Conduct of the University of Minho, as well as the applicable standards of academic integrity and data protection.

Colagem localizada em varões compósitos

RESUMO

A utilização de varões de polímero reforçado com fibras de vidro (GFRP) com redes (ou malhas) requer ligações coladas localizadas resistentes nos pontos de intersecção dos varões, repetíveis e adequadas a processos de produção automatizados. Contudo, a natureza termoendurecível da matriz, a geometria curva e a superfície entrançada dos varões tornam a ligação das interseções particularmente desafiante. Esta dissertação investigou soluções para a ligação localizada de varões entrançados de GFRP através de uma revisão das tecnologias existentes, de uma campanha experimental e de modelação numérica.

Foram avaliados oito adesivos de ligação utilizando varões de GFRP com diâmetros de 4 e 10 mm, num total de 48 provetes de interseção única. O comportamento das ligações foi analisado através da força máxima, tensão máxima de corte, deslizamento, variabilidade e modos de rotura. Para os varões de 4 mm, os adesivos 6 e 3 apresentaram as maiores tensões médias de corte, com 39,6 e 39,2 MPa, respetivamente. Para os varões de 10 mm, os maiores valores foram obtidos pelos adesivos 8 e 6, com 21,9 e 20,2 MPa. Os resultados evidenciaram ainda a influência da configuração do entrançado, das regiões ricas em resina e das condições locais de ligação na variabilidade experimental.

Foi também desenvolvido em Abaqus um modelo baseado numa zona coesiva (CZM), considerando diferentes distâncias de fixação. Para os casos experimentais selecionados, o modelo previu as forças máximas com diferenças inferiores a 10%. Globalmente, o estudo demonstra a viabilidade da ligação localizada de varões de GFRP, identificando simultaneamente a resistência da ligação, a consistência do processo e o controlo das condições superficiais e geométricas como fatores essenciais para o futuro fabrico automatizado de malhas de GFRP.

PALAVRAS-CHAVE: GFRP; varões compósitos entrançados; ligação colada localizada; redes de FRP; simulação numérica com recurso a modelos coesivos.

Localized Spot Bonding of Braided Composite Rebars

ABSTRACT

The production of glass fibre-reinforced polymer (GFRP) reinforcement grids requires strong, repeatable and automation-compatible localised bonded connections between intersecting rebars. However, the thermoset matrix, curved geometry and braided surface of the rebars make the joining of individual intersections particularly challenging. This dissertation investigated solutions for the localised bonded joining of braided GFRP rebars through a review of existing joining technologies, experimental testing and numerical modelling.

Eight adhesive materials were evaluated using 4 and 10 mm diameter GFRP rebars, comprising a total of 48 single-intersection specimens. Joint performance was assessed in terms of maximum force, maximum shear strength, slip, variability and failure behaviour. For the 4 mm rebars, adhesives 6 and 3 achieved the highest average nominal shear strengths, reaching 39.6 and 39.2 MPa, respectively. For the 10 mm rebars, the highest values were obtained with adhesives 8 and 6, reaching 21.9 and 20.2 MPa. The results further demonstrated that braid configuration, resin-rich regions and local bonding conditions contributed to the observed experimental variability.

A surface-based cohesive zone model (CZM) was also developed in Abaqus, considering different clamping distances. For the selected experimental cases, the numerical model predicted the maximum forces with differences below 10%. Overall, the investigation demonstrates the feasibility of localised joining for GFRP rebar intersections while identifying joint strength, process consistency, surface condition and geometrical control as key considerations for the future automated production of GFRP reinforcement grids.

KEYWORDS: GFRP; braided composite rebars; localised bonded joining; FRP grids; cohesive zone modelling.

TABLE OF CONTENTS

Acknowledgements iii
Resumo v
Abstract vi
List of Figures ix
List of Tables xi
List of Abbreviations and Symbols xii
2. Introduction 1
2.1. Motivation 1
2.2. Objectives 2
2.3. Dissertation Structure 2
3. FRP Grid Systems: Structural Applications, Bond Performance and Localised Joining Techniques 5
3.1. Structural Applications of FRP Grid Systems 5
3.1.1. FRP Grids in Road Construction and Buried Infrastructure 5
3.1.2. Strengthening and Seismic Rehabilitation 7
3.1.3. Aerospace Grid-Stiffened Structures 10
3.1.4. Comparative Summary of FRP Grid Applications and Studies 14
3.2. Existing Bonding Techniques 16
3.2.1. Solvent-Assisted Welding of Thermosetting Epoxy Composites 16
3.2.2. Infrared Welding of Carbon- and Glass-Fibre-Reinforced Thermoplastic Composites 17
3.2.3. Resistance Welding of Thermoset Composites Using Thermoplastic Interlayers 18
3.2.4. Ultrasonic Welding of Thermoset Composite Joints Using Thermoplastic Films and Mesh Energy Directors 19
3.2.5. Comparative Summary of Bonding Techniques 21
4. Experimental Mechanical Assessment of Bonded joints Between GFRP rebars 23
4.1. Materials 23
4.1.1. GFRP Rebars 23

4.1.2. Adhesives 26
4.2. Test Setup and Programme 32
4.2.1. Specimen Configuration and Preparation 32
4.2.2. Experimental Programme 35
4.3. Results and Discussion 36
4.3.1. Force–Slip Behaviour and Key Mechanical Results 36
4.3.2. Comparative Mechanical Performance 44
4.3.3. Failure Modes and Experimental Observations 46
4.3.4. Overall comparison of the experimental response 53
4.4. Summary 57
5. Numerical Modelling of GFRP Rebar Joints 59
5.1. Cohesive Zone Modelling Approach 59
5.2. Numerical Results and Experimental Comparison 62
5.3. Summary 65
6. Conclusions and Future Work 67
6.1. Key Findings 67
6.2. Future Work 69
References 71

LIST OF FIGURES

Figure 2-1 Steel reinforcement (left) and GFRP reinforcement (right) [1]. 6
Figure 2-2 FRP grid-UHPC pipe with external FRP jacket [2]. 7
Figure 2-3 (a) Cross-section of the strengthening approach, (b) grid winding and (c) installation of jackets [3]. 8
Figure 2-4 Specimens strengthened (a) with BFRP sheets and (b) with BFRP grids [4]..... 9
Figure 2-5 Ruptured CFRP grid strands, indicated by arrows, and spalled concrete cover [5]. 9
Figure 2-6 Strengthening schematics with (a) FRP grids and (b) FRP grids with FRP bars [6]. 10
Figure 2-7 Ariane 6 PPH Interstage 2/3 (left) and EDRS-C central cylinder structure [7]..... 11
Figure 2-8 CG1 (left) and CG2 (right) [8]. 12
Figure 2-9 CFRP grid-concrete system with PCM shotcrete [9]. 13
Figure 2-10 Specimen under fatigue testing [10]. 14
Figure 2-11 Extrinsic welding sequence: (a) activation of bond exchange, (b) untreated permanent-network surfaces, (c) solvent treatment and formation of a reactive gel layer, and (d) hot pressing, solvent removal and reformation of the covalent network [11]..... 17
Figure 2-12 Infrared welding arrangement showing local heating of the overlap, matrix softening and pressure-assisted consolidation [12]. 18
Figure 2-13 Schematic representation of resistance welding with a thermoplastic interlayer and embedded heating element [13]. 19
Figure 2-14 Schematic diagram of an ultrasonic spot-welding arrangement [15]. 20
Figure 3-1 Schematic diagram of GFRP braided rebars (Courtesy of The Light Rebar Company) 25
Figure 3-2 Bundles of 4 mm & 10 mm GFRP rebars (courtesy of The Light Rebar Company) 25
Figure 3-3 Geometry and dimensions of the single-joint GFRP specimen used in the experimental programme. 32
Figure 3-4 MTS tensile testing arrangement and fixture used for the single-joint GFRP specimens. 33
Figure 3-5 Force–slip response and joint performance of Adhesive 1 for 4 mm and 10 mm rebars..... 37
Figure 3-6 Force–slip response and joint performance of Adhesive 2 for 4 mm and 10 mm rebars..... 38

Figure 3-7 Force–slip response and joint performance of Adhesive 3 for 4 mm and 10 mm rebars..... 39
Figure 3-8 Force–slip response and joint performance of Adhesive 4 for 4 mm and 10 mm rebars..... 40
Figure 3-9 Force–slip response and joint performance of Adhesive 5 for 4 mm and 10 mm rebars..... 41
Figure 3-10 Force–slip response and joint performance of Adhesive 6 for 4 mm and 10 mm rebars..... 42
Figure 3-11 Force–slip response and joint performance of Adhesive 7 for 4 mm and 10 mm rebars..... 43
Figure 3-12 Force–slip response and joint performance of Adhesive 8 for 4 mm and 10 mm rebars..... 44
Figure 3-13 Comparison of average maximum nominal shear strength of the eight joining materials for 4 and 10 mm GFRP rebars. 53
Figure 3-14 Adhesive joint geometry for (a) 4 mm and (b) 10 mm GFRP rebars. 54
Figure 4-1 Geometry of 10 mm and 4 mm rebars clamped at (a) 30 mm, (b) 40 mm, (c) 30 mm & (d) 40 mm from joint 60
Figure 4-2 Global mesh size of 10 mm rebar (a) 4.43 mm & 4 mm rebar (b) 1.775 mm 62
Figure 4-3 Influence of clamping distance on the numerical force–slip response of the 4 mm and 10 mm GFRP joints. 63
Figure 4-4 Comparison of experimental and numerical force–slip responses for the 4 mm and 10 mm GFRP joints at a 30 mm clamping distance. 64

LIST OF TABLES

Table 2-1 Comparative summary of FRP grid applications, materials, geometrical characteristics and installation methods reported in the reviewed studies. 15
Table 2-2 Comparative summary of bonding and welding techniques for FRP composite joints, including materials, process parameters, joining mechanisms and reported joint performance. 22
Table 3-1 Summary of the main physical, mechanical and processing properties of the joining materials, according to the manufacturers' technical datasheets. 29
Table 3-2 Summary of the durability and environmental resistance characteristics of the joining materials, as reported in the manufacturers' technical datasheets. 31
Table 3-3 Experimental programme for the mechanical testing of the GFRP single-joint specimens. 35
Table 3-4 Mean mechanical response and coefficient of variation of the tested GFRP joints. 45
Table 3-5 Failure modes and experimental observations of the 4 mm GFRP rebar joints. 48
Table 3-6 Failure modes and experimental observations of the 10 mm GFRP joints. 51
Table 4-1 GFRP rebars mechanical properties 60
Table 4-2 Cohesive and damage parameters adopted for the joint interface. 61

LIST OF ABBREVIATIONS AND SYMBOLS

Abbreviations

AF	Adhesive failure
B24	Braided rebar configuration with 24 bobbin threads
B48	Braided rebar configuration with 48 bobbin threads
BFRP	Basalt Fibre-Reinforced Polymer
CF	Cohesive Failure
CFRP	Carbon Fibre-Reinforced Polymer
CoV	Coefficient of Variation
CZM	Cohesive Zone Modelling
FRP	Fibre-Reinforced Polymer
GFRP	Glass Fibre-Reinforced Polymer
LSS	Lap-Shear Strength
MF	Mixed Failure
MTS	Material Testing System
PCM	Polymer-Cement Mortar
RR	Resin-Rich
TDS	Technical Data Sheet
UHPC	Ultra-High-Performance Concrete

Symbols

A	Cross-sectional area of rebar
d	Rebar diameter
E	Elastic modulus
E_l	Longitudinal elastic modulus
F	Applied force
F_{max}	Maximum force
G	Shear modulus
K_{nn}	Normal cohesive stiffness
K_{ss},K_{tt}	Shear cohesive stiffnesses

L	Gauge/reference length
s	Joint slip
u	Measured displacement
ΔL	Elastic elongation of rebar
v, Nu	Poisson's ratio
τ_{max}	Maximum nominal shear strength

THIS PAGE WAS INTENTIONALLY LEFT BLANK

1. INTRODUCTION

1.1. Motivation

Fibre-reinforced polymer (FRP) reinforcement has emerged as an alternative to conventional steel reinforcement in applications where corrosion resistance, low self-weight and long-term durability are important. Among the available systems, glass fibre-reinforced polymer (GFRP) rebars offer high tensile strength, low thermal conductivity and electromagnetic neutrality while avoiding the corrosion-related deterioration associated with steel reinforcement. These characteristics make GFRP particularly attractive for concrete structures exposed to aggressive environments and for applications where reduced maintenance and extended service life are required.

The use of GFRP reinforcement in the form of prefabricated grids or meshes can provide additional advantages by simplifying reinforcement placement and enabling more efficient and repeatable construction. However, the manufacture of such grids requires reliable connections at the intersections between orthogonally positioned rebars. Unlike steel reinforcement, for which “welding” is an established industrial process, joining cured thermoset GFRP rebars is considerably more challenging because the polymer matrix cannot simply be remelted and fused. The curved and textured surface of braided rebars (used in the context of this work), together with the small and localized contact region at an intersection, further complicates the development of a consistent joint.

Different approaches may potentially be adapted for this purpose, including adhesive bonding and joining technologies based on thermoplastic interfaces, resistance heating or ultrasonic energy. The principal challenge is not only to obtain sufficient interfacial strength, but also to achieve consistent bond quality while avoiding damage to the composite reinforcement and maintaining a process suitable for industrial production.

Accordingly, this dissertation investigates the localized spot bonding of braided GFRP rebars, with particular emphasis on identifying suitable joining technologies and materials and evaluating the mechanical behaviour of individual grid intersections. The work combines a review of existing FRP grid applications and composite joining technologies with an

experimental investigation of different joining materials and a numerical assessment of the joint response. Particular attention is given to the influence of rebar diameter, joining material, surface condition and local joint characteristics, with the broader aim of supporting the development of a reliable and repeatable joining process for future automated manufacture of GFRP reinforcement grids.

1.2. Objectives

The main objectives of this MSc dissertation are:

1. Identify spot welding technologies compatible for localised application in GFRP rebars.
2. Identify suitable matrices for the mentioned technologies.
3. Develop prototypes for validation purposes.
4. Shortlist recommended industrially viable solutions based upon objectives 1–3.

These objectives establish a progression from the identification of potential joining technologies and compatible material systems to their practical implementation and validation. The work ultimately aims to provide a technical basis for selecting joining solutions that combine adequate mechanical performance with the processing characteristics required for the industrial production of braided GFRP reinforcement grids.

1.3. Dissertation Structure

This MSc dissertation is organised into five chapters, as follows.

Chapter 1 – Introduction presents the motivation for investigating localised joining of braided GFRP rebars, defines the main objectives of the research and outlines the structure of the dissertation.

Chapter 2 – FRP Grid Systems: Structural Applications, Bond Performance and Localised Joining Techniques establishes the background to the investigation. The first part reviews applications of FRP grid systems in civil infrastructure, strengthening, seismic rehabilitation and lightweight structures, together with relevant aspects of bond behaviour and durability. The second part examines joining technologies potentially applicable to composite grid intersections, including solvent-assisted, infrared, resistance and ultrasonic welding.

Particular attention is given to their joining mechanisms, processing requirements, achievable joint performance and potential for localised and automated application.

Chapter 3 – Experimental Programme presents the materials, specimen preparation, testing methodology and experimental results. Braided GFRP rebars with nominal diameters of 4 and 10 mm are investigated using eight different joining materials. A total of 48 single-intersection specimens are mechanically tested and assessed through their force–slip behaviour, maximum force, shear strength, slip at maximum force, repeatability and failure mechanisms. The chapter also examines the influence of variations in the braided rebar surface and local bonding conditions on the measured response.

Chapter 4 – Numerical Modelling of GFRP Rebar Joints develops a three-dimensional numerical representation of the single-intersection joint using a surface-based cohesive zone modelling approach in Abaqus. The influence of horizontal-rebar clamping distance is investigated, and the numerical force–slip response is subsequently compared with representative experimental results for the 4 and 10 mm rebars. The chapter evaluates the capability and limitations of the simplified numerical approach in reproducing the experimentally observed joint behaviour.

Chapter 5 – Conclusions and Future Work summarises the principal findings obtained throughout the dissertation and evaluates them in relation to the original research objectives. The chapter identifies the most relevant outcomes for the development of localised GFRP rebar joining, discusses the limitations of the present investigation and proposes future work towards improving joint repeatability, refining the numerical model, assessing durability and progressing from individual intersections towards automated manufacture and validation of complete GFRP reinforcement grids.

THIS PAGE WAS INTENTIONALLY LEFT BLANK

2. FRP GRID SYSTEMS: STRUCTURAL APPLICATIONS, BOND PERFORMANCE AND LOCALISED JOINING TECHNIQUES

2.1. Structural Applications of FRP Grid Systems

Fibre-reinforced polymer (FRP) grids are increasingly used in structural applications where corrosion resistance, low self-weight and ease of handling are central design considerations. In civil infrastructure, they provide an alternative to steel reinforcement in aggressive environments, while in aerospace structures they enable lightweight, integrated load-bearing layouts. Their behaviour is governed not only by the fibre type, such as glass, carbon or basalt, but also by grid spacing, strand geometry, surface condition and the way the grid is connected to concrete, mortar or a polymer matrix.

The following subsections organise the reviewed studies according to their main field of application and the structural problem addressed. This helps clarify how the same grid concept has been adapted for pavement reinforcement, buried infrastructure, structural strengthening, seismic rehabilitation, aerospace components and durability assessment.

2.1.1. FRP Grids in Road Construction and Buried Infrastructure

In road infrastructure, Chen et al. [1] reported one of the early field applications of GFRP reinforcement in continuously reinforced concrete pavement (CRCP). The pavement test sections were constructed on Route 9 in Martinsburg, West Virginia, USA, and the application was reported in 2008. The GFRP reinforcement was not a prefabricated grid; instead, longitudinal and transverse rebars were tied in situ using plastic zip ties to form a grid-like reinforcement cage. The GFRP section used 22.2 mm diameter longitudinal bars spaced at 152.4 mm, whereas the reference steel section used 19.1 mm diameter bars at the same spacing, with transverse reinforcement placed at 1.2 m (see Figure 2-1). After 38 days, the GFRP section developed 40 transverse cracks with an average spacing of 3.31 m, compared with 75 cracks and 1.71 m spacing in the steel section. Although the lower stiffness of GFRP produced slightly wider cracks, the maximum crack width was 0.86 mm, remaining below the AASHTO limit of 1.0 mm. These results show that GFRP reinforcement can reduce crack frequency in CRCP while providing a corrosion-free alternative for pavement applications.



Figure 2-1 Steel reinforcement (left) and GFRP reinforcement (right) [1].

For buried infrastructure, Liao et al. [2] published an experimental study in 2023, from Dongguan University of Technology and Guangdong University of Technology, China, on FRP grid-reinforced ultra-high-performance concrete (UHPC) pipes. The work was a laboratory investigation rather than a field installation, and it focused on pipe systems for municipal water networks, sewage systems and underground tunnels. The proposed pipe consisted of a UHPC shell reinforced internally with an FRP grid cage, where CFRP bundles were placed in the hoop direction and GFRP bundles in the transverse direction at the middle of the pipe wall. Fifteen specimens were tested under lateral compression to examine the influence of grid reinforcement, wall thickness and external CFRP jacketing. The internal grid increased the initial cracking load by about 30%, from 23 kN to 30 kN, and improved post-cracking resistance, while increasing the wall thickness from 30 mm to 45 mm raised ring stiffness by 422% and increased the ultimate load to 140-230 kN. A one-ply external CFRP jacket added a further 115% increase in ring stiffness as shown in Figure 2-2 FRP grid-UHPC pipe with external FRP jacket [2]. and helped prevent separation between the FRP grid and the UHPC cover. The work demonstrates how FRP grids can contribute to thin, durable and lightweight pipe systems without compromising the stiffness required for buried service conditions.



Figure 2-2 FRP grid-UHPC pipe with external FRP jacket [2].

2.1.2. Strengthening and Seismic Rehabilitation

Gao et al. [3], from Gandong Vocational and Technical College, Fuzhou, Jiangxi, China, reported an experimental study in 2026 on reinforced-concrete columns with corroded stirrups strengthened using a combined CFRP grid and GFRP jacket system. The problem addressed is important because stirrup corrosion reduces concrete confinement, weakens the restraint against longitudinal bar buckling and may shift column failure towards a brittle compression mode. The authors tested four unstrengthened and thirteen strengthened short-column specimens under axial compression, considering stirrup corrosion levels of 0%, 10%, 20% and 30%, together with different numbers of CFRP grid layers. The strengthening system used a thin bidirectional CFRP grid, with approximately 20 mm longitudinal spacing and 5 mm transverse strip width, placed with epoxy-based grout inside an external GFRP jacket. Compared with the unstrengthened corroded columns, the hybrid system improved confinement, axial load capacity and deformation resistance. The GFRP jacket alone increased ductility by up to 45.8%, while adding CFRP grids raised the improvement to 74.8%. Further grid layers increased bearing capacity and ductility, although the incremental gain reduced with each additional layer. The results indicate that CFRP grids and GFRP jackets shown in Figure 2-3 can act together as a lightweight repair system, combining the stiffness of CFRP with the deformability and confinement provided by GFRP.

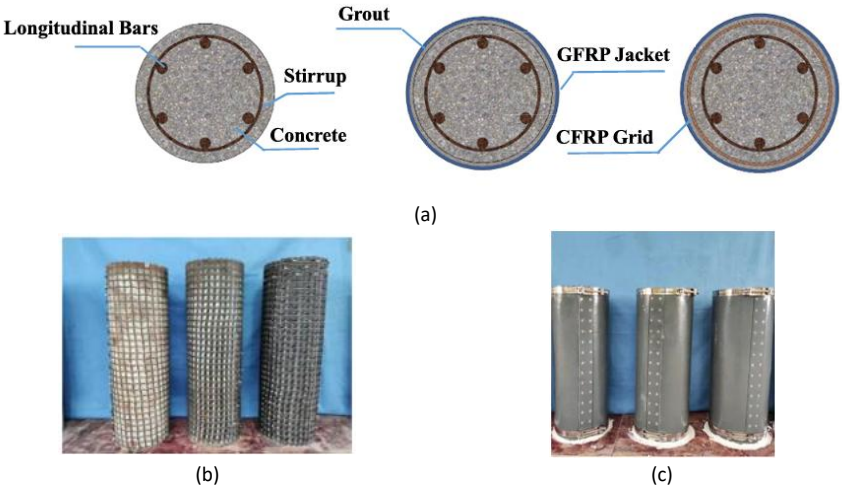


Figure 2-3 (a) Cross-section of the strengthening approach, (b) grid winding and (c) installation of jackets [3].

Liu et al. [4], from Southeast University, Southwest Petroleum University and Xihua University, China, published an experimental study in 2025 on BFRP grids used as external confinement for concrete columns under axial compression. The work responds to the need for repair systems that can improve the load-bearing capacity and ductility of ageing or poorly confined columns while reducing dependence on continuous bonded sheets, which may be affected by voids, bond defects and long-term adhesive degradation. The authors tested 27 concrete cylinders, including 18 strengthened specimens and 9 controls, and examined specimen size, number of BFRP grid layers and performance relative to BFRP sheet confinement shown in Figure 2-4. The BFRP grids had 50 x 50 mm spacing, 8 mm rib width and 1 mm thickness, and were wrapped around the columns within a mortar encasement. Two grid layers increased compressive capacity by more than 35% and improved axial strain capacity by up to 120%, changing the response from brittle crushing to a more gradual failure mode. A third layer gave only limited additional strength because delamination developed between the strengthening layer and the concrete surface. Compared with BFRP sheets, the grids produced a smaller increase in peak strength but a more stable post-peak response, partly because the nylon-tied intersections allowed local deformation. This makes BFRP grids a useful option where ductility and deformation capacity are priorities.



(a) (b)

Figure 2-4 Specimens strengthened (a) with BFRP sheets and (b) with BFRP grids [4].

Christou et al. [5], from Frederick University, Cyprus, published a numerical and analytical study in 2013 on how CFRP grid and CFRP wrap confinement influence the interaction diagrams of circular reinforced-concrete sections under combined axial load and bending. Interaction diagrams are commonly used in column design, but the contribution of FRP confinement is often simplified or omitted, which can lead to conservative assessment. The authors compared an unconfined RC section, light confinement using an embedded CFRP grid and heavier confinement using CFRP wraps with thicknesses of 1.5 mm and 2.5 mm. The CFRP grid had approximately 69% open area and strand spacings of 45.7 mm and 40.6 mm in the two directions, allowing it to be embedded in concrete and formed into a tubular shape. Light grid confinement increased the maximum compressive axial capacity by about 25%, while heavy CFRP wrapping increased it by up to 500%. The maximum moment capacity also increased, by about 17% for the grid and up to 335% for the wraps. The confinement effect was strongest in the compression-controlled region, where concrete crushing governs failure, and more limited in the tension-controlled region as shown in Figure 2-5. The comparison shows that embedded CFRP grids can improve confinement and ductility, whereas full wraps are more suitable when large strength gains are required.



Figure 2-5 Ruptured CFRP grid strands, indicated by arrows, and spalled concrete cover [5].

Lu et al. [6], from Southeast University and Nanjing Forestry University, China, presented a combined experimental and numerical study in 2026 on the seismic design of RC columns strengthened with FRP grids, embedded FRP bars and cement-based jacket materials (see Figure 2-6). The work addresses existing columns that may have limited ductility and large residual deformation after earthquakes, making post-earthquake repair difficult. A multi-objective optimisation framework was developed in OpenSees and MOEA/D to balance three design targets: increasing ductility, reducing residual drift and controlling strengthening cost. The framework was validated through low-cycle cyclic tests on five circular RC columns, including one unstrengthened reference column and four columns strengthened with BFRP grids, BFRP bars and PCM overlays. The optimisation also considered CFRP and GFRP grids and bars, together with jacket materials such as PCM, ECC, UHPC and geopolymer mortar. The BFRP grid-ECC system increased ductility by about 26.4% compared with the reference BFRP grid-PCM retrofit, while CFRP grid-and-bar systems reduced residual drift by up to 32.1%. By linking experimental behaviour with numerical optimisation, the study provides a practical basis for selecting FRP grid-and-bar strengthening systems according to both structural performance and cost.

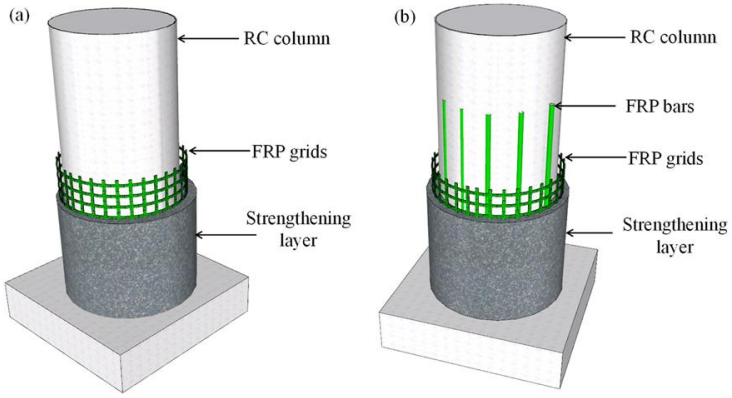


Figure 2-6 Strengthening schematics with (a) FRP grids and (b) FRP grids with FRP bars [6].

2.1.3. Aerospace Grid-Stiffened Structures

The grid concept also extends beyond civil engineering. Pavlov et al. [7], from ATG Europe, The Netherlands, presented a conference paper in 2016 at the 16th European Conference on Spacecraft Structures, Materials and Environmental Testing in Toulouse, France, on CFRP grid-stiffened and lattice structures for space applications. The work focused on launcher interstages and satellite central cylinders, where high stiffness must be achieved with minimum structural mass, cost and production time. The authors developed a semi-

automated optimisation approach and a one-shot manufacturing process based on continuous-tow prepreg fibre placement. This allowed ribs, nodes, load-introduction regions, attachment points and local cut-out reinforcement to be integrated during a single layup and curing cycle. Two aerospace design cases were considered: the Ariane 6 PPH Interstage 2/3 and the EDRS-C satellite central cylinder (see Figure 2-7). The optimised Ariane 6 interstage weighed 1033 kg, about 25% below the given mass budget of 1380 kg. For the EDRS-C central cylinder, the lattice configuration reduced mass by 27%, manufacturing cost by 30% and lead time by 20% compared with the existing CFRP/aluminium honeycomb sandwich structure. These outcomes highlight the value of CFRP grids where multiple load paths, integrated attachments and weight-efficient manufacturing are required.

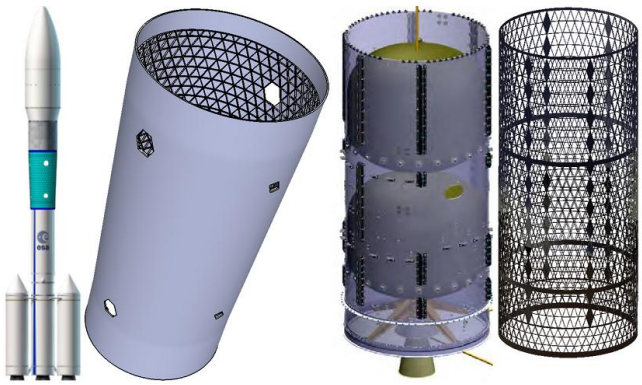


Figure 2-7 Ariane 6 PPH Interstage 2/3 (left) and EDRS-C central cylinder structure [7].

Schmidt and Hegger [8], from the Institute of Structural Concrete at RWTH Aachen University, Aachen, Germany, published an experimental study in 2025 on bond behaviour and crack development in concrete members reinforced with carbon textile grids under static and cyclic tensile loading. The work is important for serviceability design because non-metallic textile reinforcement allows thinner, corrosion-resistant concrete members, but crack control depends strongly on the bond between the yarns and the surrounding concrete. Two CFRP grids were examined: an epoxy-impregnated grid with oval yarns and 38 mm spacing (CG1), and a polystyrene-impregnated grid with nearly circular yarns and 50 mm spacing (CG2) shown in Figure 2-8. The specimens were tested under uniaxial tension, with fibre optic sensors used to measure reinforcement strain and digital image correlation used to monitor cracking. CG1 produced more closely spaced cracks, smaller crack widths and shorter transfer

lengths, whereas CG2 transferred stress less effectively and produced wider cracks over longer transfer zones. After 200,000 loading cycles, single-crack widths increased by approximately 50%, indicating progressive weakening of the yarn-concrete bond. The findings show that grid geometry, impregnation material and yarn intersections are central to crack control in carbon-grid-reinforced concrete members.

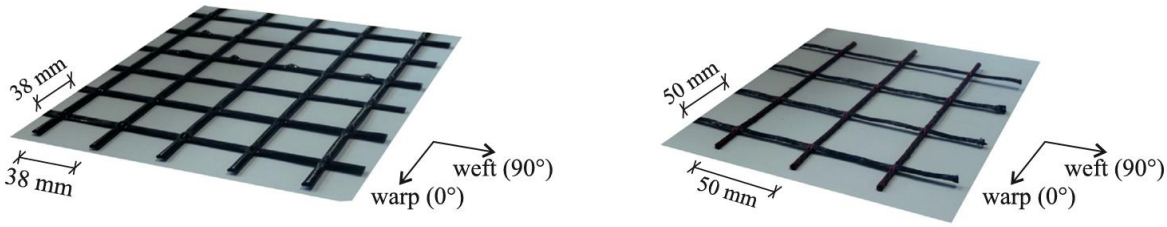


Figure 2-8 CG1 (left) and CG2 (right) [8].

Guo et al. [9], from Southwest Jiaotong University, Chengdu, China, and Kyushu University, Fukuoka, Japan, published an experimental study in 2018 on the bond behaviour and stress-transfer mechanism of CFRP grids fixed to concrete using polymer-cement mortar (PCM) shotcrete. The method was proposed as a thinner alternative to conventional concrete jacketing and as a more durable option than epoxy-bonded FRP sheets in wet, low-temperature or fire-exposed conditions. In the tested system, a CFRP grid was placed on the concrete surface and covered with a PCM shotcrete layer of about 10-20 mm shown in Figure 2-9. Six specimen types were examined by varying the number of grid points, grid spacing of 50 x 50, 75 x 75 and 100 x 100 mm, the presence of adjacent vertical grids and the type of PCM. Tensile force was transferred through successive grid points into the PCM and concrete, while the horizontal grid members provided mechanical interlock. Larger grid spacing caused a greater proportion of load to concentrate at the first grid point, increasing the first-point strain share from 44.2% at 50 mm spacing to 56.1% at 100 mm spacing. At least two active grid points were required for reliable anchorage, and specimens with adjacent axial grids and high-strength PCM showed better bond performance. Low-elasticity PCM improved deformation compatibility but was more prone to premature peeling when interface stresses exceeded the concrete-PCM bond capacity. The study therefore clarifies how grid spacing, intersection arrangement and mortar properties govern anchorage in CFRP grid-PCM strengthening systems.

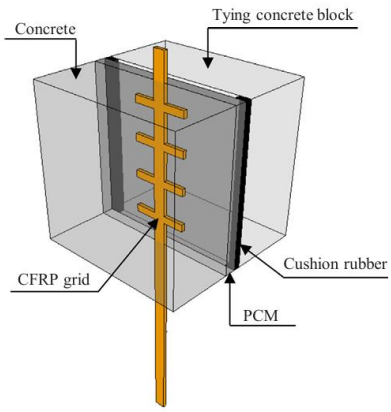


Figure 2-9 CFRP grid-concrete system with PCM shotcrete [9].

Di Tommaso et al. [10], with researchers from Italian universities and Northumbria University, United Kingdom, published an experimental study in 2017 on the durability of GFRP textile grids exposed to alkaline ageing and tension-tension fatigue loading shown in Figure 2-10. GFRP grids are widely considered for masonry and concrete strengthening because of their lower cost and compatibility with weak substrates, but glass fibres can degrade in alkaline environments, particularly under repeated service loading. The tested grids were made from ECR-glass fibres impregnated with epoxy-vinylester resin and had a regular 66 x 66 mm mesh size. Specimens were conditioned for 720 h in a Ca(OH)2 alkaline solution with 0.16% concentration by weight and then subjected to fatigue loading at 7.5 Hz, with maximum loads between 1 kN and 2.5 kN for up to 1,000,000 cycles. At 2.5 kN, unconditioned specimens failed after about 38,546-50,553 cycles, while aged specimens failed earlier, after about 23,539-26,942 cycles. At 2 kN, one unconditioned specimen survived without rupture, whereas aged specimens failed after 28,045 and 232,661 cycles. At 1 kN, most specimens showed little or no failure even after 1,000,000 cycles. Failure generally occurred near the grid joints, where fibre deviation and stress concentration were more severe. These results emphasise that chemical ageing and cyclic loading should be assessed together when designing GFRP grid strengthening systems for long-term exposure.



Figure 2-10 Specimen under fatigue testing [10].

2.1.4. Comparative Summary of FRP Grid Applications and Studies

Table 2-1 summarises the FRP grid studies reviewed in this section, including their application field, reinforcement material, grid geometry, strand diameter or thickness, surface treatment and installation method. The comparison shows that FRP grids are not a single standardised reinforcement product; instead, their form is adapted to the structural purpose. Civil infrastructure applications mainly use GFRP or hybrid FRP systems for corrosion resistance and ease of handling, strengthening studies often rely on CFRP or BFRP grids for confinement and stress transfer, and aerospace applications exploit CFRP lattice systems for high stiffness-to-weight efficiency.

The table also shows that geometry strongly influences performance. Closely spaced textile grids are preferred for crack control and bond development, while thicker grids, wraps or jackets are used when confinement and load-bearing capacity are the main objectives. The installation method is equally important: some systems are mechanically assembled, others are embedded in concrete or mortar, and some rely on external wrapping or integrated manufacturing. Across the reviewed studies, durability, bond transfer and long-term performance remain key design concerns, especially for GFRP grids exposed to alkaline environments, cyclic loading or repeated service actions.

Table 2-1 Comparative summary of FRP grid applications, materials, geometrical characteristics and installation methods reported in the reviewed studies.

Ref.	System	Application	Spacing (mm)	d/t (mm)	Fibre (%)	Surface	Installation
[1]	In-situ rebar grid (GFRP and steel)	CRCP pavement	152.4 longitudinal x 1200 transverse	22.2 GFRP; 19.1 steel (d)	70	None	Mechanical assembly with zip ties
[2]	Internal CFRP/GFRP grid with CFRP jacket	UHPC pipe reinforcement	10.6 x 10.6; bundle width 3.3	0.3 bundle (t)	N/S	None	Co-cast grid with epoxy-bonded wrap
[3]	CFRP sheet grid with GFRP jacket	Repair of corroded RC columns	20 longitudinal x 5 transverse	0.3 (t)	N/S	Specialised coating	Epoxy grout and external jacket
[4]	BFRP sheet grid	Axial strengthening of concrete columns	50 x 50; strip width 8	1 (t)	N/S	Surface roughening	Wrapped grid with mortar encasement
[5]	Embedded CFRP grid and external CFRP wraps	RC column confinement under axial load and bending	45.7 longitudinal x 40.6 transverse	1 grid strand; 1.5 and 2.5 wraps (t)	N/S	None	Embedded grid and external wrapping
[6]	FRP grids, embedded bars and cementitious jacket (BFRP/CFRP/GFRP)	Seismic strengthening of RC columns	Bidirectional external grid	1 and 3 (t)	N/S	None	Embedded reinforcement with cementitious bonding
[7]	CFRP grid-stiffened lattice	Launcher and satellite structures	Not reported (orthogrid)	N/S	63	None	Integrated one-shot manufacture
[8]	CFRP textile grids: epoxy-impregnated CG1 and polystyrene-impregnated CG2	Concrete tension members	38 x 38 (CG1); 50 x 50 (CG2)	3.09 (CG1); 2.83 (CG2) (d)	N/S	None	Mechanical interlock
[9]	CFRP grid with PCM	RC strengthening	50 x 50, 75 x 75 and 100 x 100	3 (t)	N/S	None	Mechanical anchorage through grid and PCM
[10]	GFRP textile grid	Masonry strengthening and durability	66 x 66	Equivalent thickness 3	N/S	None	Mechanical interlock

2.2. Existing Bonding Techniques

After reviewing structural applications of FRP grids, the next step is to examine how composite components can be joined. This is particularly important for GFRP grid systems, where the intersection between two rebars must be strong, repeatable and suitable for localised production. Cured thermoset composites cannot be remelted in the same way as thermoplastics, so several approaches have been developed to create either a reactive surface or a weldable thermoplastic interface. The following section reviews solvent-assisted welding, infrared welding, resistance welding with thermoplastic interlayers and ultrasonic welding using films or mesh energy directors. The discussion focuses on the working principle, material system, processing conditions, joint performance and suitability for local joining of composite grid intersections.

2.2.1. Solvent-Assisted Welding of Thermosetting Epoxy Composites

An et al. [11], from Xi'an Jiaotong University, China, published an experimental study in 2022 on solvent-assisted extrinsic welding of conventional thermosetting epoxy composites. The challenge addressed in this work is that cured epoxy forms a permanent covalent network, which gives thermal stability but prevents direct melting and chain diffusion. The laminates were made from DGEBA epoxy cured with glutaric anhydride and DMP-30, reinforced with 3K plain-woven carbon fabric in the 0 degrees/90 degrees directions. The composites were 2 mm thick, contained 40 wt% epoxy and had a glass-transition temperature of 84.5 degrees C. To reactivate the surface, the joint regions were immersed for 15 min in ethylene glycol containing a TBD catalyst at 140 degrees C, forming a thin reactive gel layer. Single-lap specimens with a 10 mm overlap were then hot-pressed at 200 degrees C and 600 kPa (see Figure 2-11), allowing chain diffusion and covalent bond reformation across the interface. The treatment increased joint strength from 5.2 MPa for untreated specimens to 22.2 MPa after immersion and 30 min welding, while 12 h of welding increased the strength to 28.5 MPa. The method demonstrates that fully cured thermoset composites can be joined through controlled surface reactivation rather than mechanical fastening or conventional adhesive bonding. For local GFRP grid intersections, however, the solvent treatment, catalyst, elevated temperature and long processing time would make direct implementation difficult.

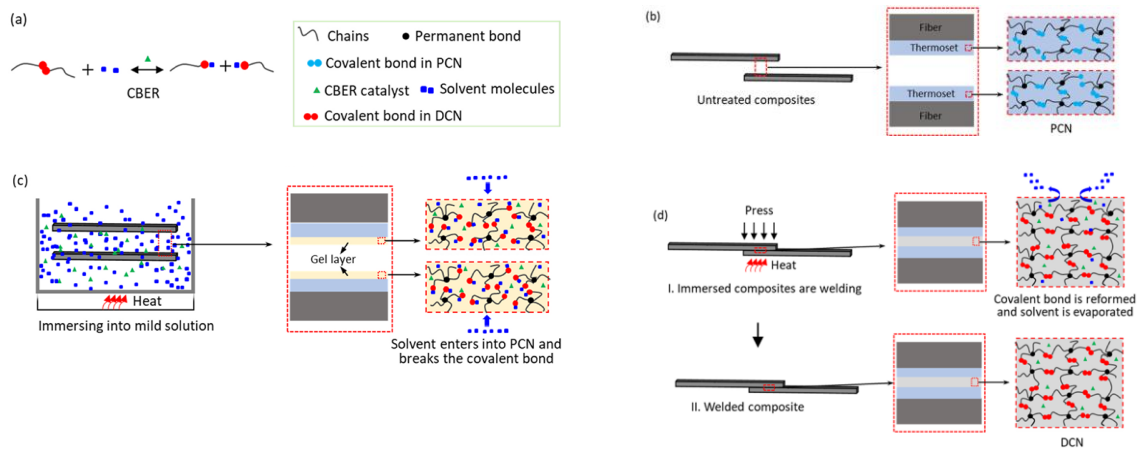


Figure 2-11 Extrinsic welding sequence: (a) activation of bond exchange, (b) untreated permanent-network surfaces, (c) solvent treatment and formation of a reactive gel layer, and (d) hot pressing, solvent removal and reformation of the covalent network [11].

2.2.2. Infrared Welding of Carbon- and Glass-Fibre-Reinforced Thermoplastic Composites

Campos et al. [12], from the Federal University of Itajuba, Brazil, with collaborators in France, published an experimental study in 2026 on infrared welding of carbon- and glass-fibre-reinforced Elium 150 thermoplastic composites. The work considers a non-contact fusion-bonding route for thermoplastic composites, which can be remelted and joined without adhesives as shown in Figure 2-12. The acrylic Elium 150 matrix was mixed with 1.2 wt% Luperox 78 initiator and reinforced with either five plies of 6K woven carbon fabric or ten plies of woven E-glass fabric, both arranged in the 0 degrees/90 degrees direction. The 2 mm laminates were manufactured by vacuum-assisted resin transfer moulding. Thermal characterisation gave a glass-transition temperature of 94.16 degrees C and showed degradation onset near 204 degrees C. During welding, a 1000 W quartz-halogen infrared lamp heated the overlap region for 180 s, followed by 10 min of consolidation under 0.4 or 0.5 MPa pressure. The best condition was 150 degrees C and 0.5 MPa, giving lap-shear strengths of 9.59 MPa for carbon-fibre/Elium and 13.72 MPa for glass-fibre/Elium composites. The better performance of the glass-fibre joints was associated with improved fibre-matrix compatibility, while carbon-fibre specimens showed more interfacial failure and resin leakage. Infrared welding therefore offers a clean, contactless route for thermoplastic composite joining, but the results also show that increasing heat or pressure beyond the optimum can reduce joint quality by promoting excessive resin flow.

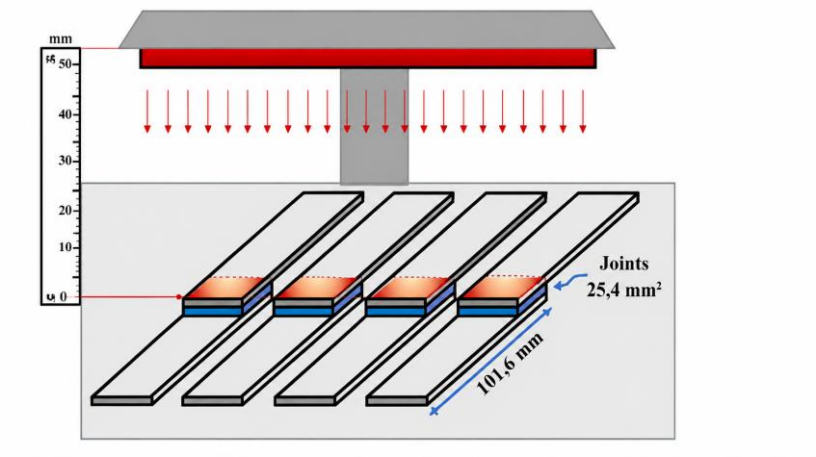


Figure 2-12 Infrared welding arrangement showing local heating of the overlap, matrix softening and pressure-assisted consolidation [12].

2.2.3. Resistance Welding of Thermoset Composites Using Thermoplastic Interlayers

Resistance welding is commonly associated with thermoplastic composites, but it can be extended to thermoset laminates when a compatible thermoplastic layer is introduced at the surface. In a 2024 review, Stankiewicz et al.[13], from the Lukasiewicz Research Network-Institute of Aviation, Warsaw, Poland, noted that cured thermoset composites cannot be remelted because of their cross-linked structure; therefore, they require a co-cured thermoplastic film or an intermediate thermoplastic layer before welding. Maierhofer et al. [14] experimentally applied this concept in 2024 through a study involving the University of Bath, GKN Aerospace and Politecnico di Milano. Their specimens were 14-ply IM7/8552 carbon-fibre/epoxy thermoset laminates with a 0.25 mm PEI film co-cured onto the laminate surface, forming a thermoplastic-rich coupling layer. During welding, current passed through a stainless-steel mesh heating element insulated with glass-fibre/PEI layers, producing local heat at the joint interface (see Figure 2-13). A processing window of 300-325 degrees C, 0.85-1.05 MPa and 25-50 s was recommended. Within this range, the welded joints achieved Mode I fracture toughness comparable to high-performance CF/PEI thermoplastic composites and about 290% higher than the reference thermoset joint. This approach is promising for automated joining because it creates a fusion-bonded interface without long adhesive curing cycles, although the processing window is narrow: insufficient heat or pressure causes poor fusion, whereas excessive temperature, time or pressure may lead to porosity, resin loss and thermal degradation.

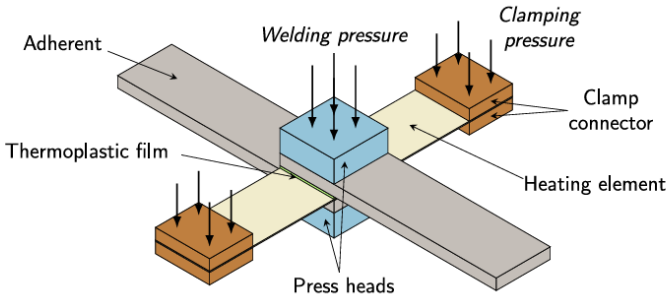


Figure 2-13 Schematic representation of resistance welding with a thermoplastic interlayer and embedded heating element [13].

2.2.4. Ultrasonic Welding of Thermoset Composite Joints Using Thermoplastic Films and Mesh Energy Directors

Meram [15] presented a conference paper in 2025 at the 7th International Congress on Engineering and Sciences in Istanbul, Turkiye, discussing the main challenges and limitations of ultrasonic welding for thermoplastic composites. Ultrasonic welding is a fast and clean fusion-bonding method because it uses localised vibration-induced heating rather than adhesives, fasteners or large external heating zones. The process converts high-frequency electrical current into mechanical vibration, generally between 20 and 70 kHz, and transmits it through the sonotrode to the joint interface as shown in Figure 2-14. Frictional heating first develops at the contact surface, followed by viscoelastic heating of the polymer; once the interface softens, pressure promotes wetting, resin flow and molecular diffusion, and the joint consolidates during cooling. Despite its short cycle time and automation potential, the process is sensitive to laminate thickness, stiffness, damping behaviour, amplitude, pressure, holding time and energy director geometry. These factors make parameter selection material- and geometry-specific, which is particularly relevant for composite grid intersections where the contact area is small and local overheating or fibre disturbance must be avoided.

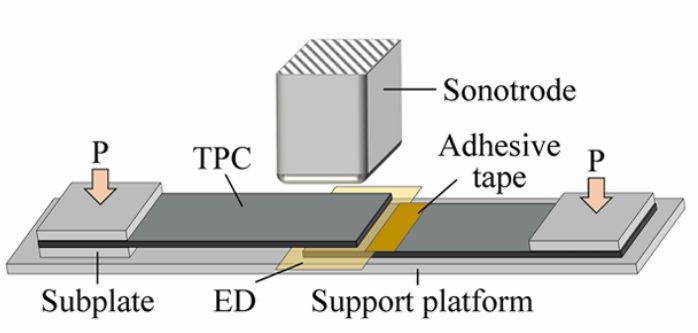


Figure 2-14 Schematic diagram of an ultrasonic spot-welding arrangement [15].

Li et al. [16], from Chengdu Aircraft Industrial Group, Chengdu, China, and Yue et al. [17], from Shandong University, Jinan, China, published two closely related experimental studies in 2026 and 2025, respectively, on ultrasonic welding of carbon-fibre-reinforced thermoplastic composites using woven thermoplastic mesh energy directors. Both works addressed the limitations of conventional film energy directors, which can produce non-uniform heat generation, resin squeeze-out and local defects at the weld interface. Li et al. used CF/PEEK laminates with a plain-woven PEEK mesh, while Yue et al. used CF/PPS laminates with a plain-woven PPS mesh. In both cases, the mesh was approximately 200 µm thick, made from 100 µm filaments and had a 37% open area. The filament crossings acted as distributed heat-generation points, while the open areas allowed resin flow, air removal and more uniform interface consolidation. For CF/PEEK joints, the optimum spot-welding condition was 80 µm amplitude, 800 N force and 550 ms welding time, giving a lap-shear strength of 40.3 MPa with only 0.12% defect area. For CF/PPS joints, the optimum condition was 70 µm amplitude, 500 N force and 0.12-0.13 mm welding displacement, producing a maximum lap-shear strength of 32.6 MPa and a minimum defect level of 1.1%. Yue et al. also showed that the CF/PPS joints retained almost the same strength after 12 weeks at 80 degrees C and 95% relative humidity. Together, these studies show that woven mesh energy directors can improve heat distribution and weld reliability compared with flat films, although excessive welding time, amplitude or displacement can still cause overheating, voids and fibre deformation.

Yao et al. [18], from Tiangong University and the Tianjin Key Laboratory of Advanced Mechatronics Equipment Technology, China, published a combined experimental and numerical study in 2026 on process stability in continuous ultrasonic welding of CF/PA66

thermoplastic composites. Although the work concerns continuous rather than spot welding, it explains an important heat-control issue that is also relevant to localised welding. Finite element analysis showed that viscoelastic heat generation is delayed at the start of welding and then accumulates towards the end of the joint. Constant welding speeds of 10, 15 and 20 mm/s could not fully balance this behaviour: lower speeds improved early bonding but increased the risk of over-welding later, while higher speeds reduced heat input and caused weak bonding at the beginning. The authors therefore proposed variable-speed strategies, including uniform acceleration, step variation and exponential variation. Uniform acceleration was the most effective strategy, particularly when the speed increased from 10 to 15 mm/s, improving weld quality uniformity by 27.96% and reaching a maximum lap-shear strength of 15.72 MPa. The work reinforces that ultrasonic welding quality depends not only on material choice and energy director geometry, but also on how vibration energy is delivered over time. For GFRP grid intersections, this supports careful control of welding energy, time, pressure and contact geometry.

2.2.5. Comparative Summary of Bonding Techniques

Table 2-2 compares the bonding and welding techniques reviewed in Section 2.2, focusing on material system, specimen geometry, bonding area, process parameters, joining mechanism and reported joint performance. Both thermoset- and thermoplastic-based composite joints are included because the objective is to identify techniques that could be adapted for localised joining of GFRP grid intersections. The table should therefore be read as a process comparison rather than a direct ranking of strength values, since the studies used different materials, joint geometries, loading modes and testing methods.

The comparison shows that each technique creates the joint interface in a different way. Solvent-assisted welding can generate strong covalent bonding in thermoset composites, but it requires chemical activation, elevated temperature and long processing times. Infrared welding is cleaner and non-contact, although its performance depends strongly on controlling the molten layer and avoiding resin leakage. Resistance welding becomes suitable for thermoset composites only when a thermoplastic interlayer is introduced, and its processing window must be carefully controlled to avoid incomplete fusion or thermal damage.

Ultrasonic welding offers the shortest cycle time and the clearest potential for localised spot joining, especially when mesh energy directors are used to improve heat distribution and reduce defects. However, most available evidence still comes from flat laminates or continuous welding studies. The joining of curved GFRP rebars, the small contact area at grid intersections and the durability of welded nodes under repeated loading remain open issues that justify further investigation.

Table 2-2 Comparative summary of bonding and welding techniques for FRP composite joints, including materials, process parameters, joining mechanisms and reported joint performance.

Ref.	Specimen	Area / fibre (%)	Material	Parameters	Technique	Mechanism	LSS (MPa)
[11]	Single-lap joint (50 x 20 x 2)	200 / 60	CF/epoxy (thermoset), EG solvent, TBD catalyst	Immersion: 140 degrees C, 15 min; hot press: 200 degrees C, 0.6 MPa, 30 min	Extrinsic welding	Covalent bond exchange, interdiffusion	22.2
[12]	Single-lap joint (101.6 x 25.4 x 2)	645.16 / CF: 53; GF: 39	CF/Elium® 150 & GF/Elium® 150 (thermoplastic acrylic resin)	T: 150-200 degrees C; heating time: 180 s; press time: 10 min; P: 0.4-0.5 MPa	Infrared welding	Polymer softening, chain interdiffusion, consolidation under pressure	9.59 (CF), 13.72 (GF)
[14]	DCB specimen (160×21×2)	N/S	CF/epoxy (thermoset), PEI film (thermoplastic), stainless steel mesh, GF/PEI insulation	T: 300-325 degrees C; t: 25-50 s; P: 0.85-1.05 MPa	Resistance welding	Thermoplastic melting, interdiffusion, gradient interphase, mesh heating	N/S
[15]	Overlap joint, N/S	N/S, (50)	Thermoplastic CFRP (PEEK, PPS, PEKK)	f: 20-70 kHz; A: 50-70 µm; t: 1-3 s; P: 0.2-0.6 MPa	Ultrasonic welding	Friction, viscoelastic heating, fusion bonding	LSS +19%; welding time -40% compared with hot press
[16]	Single-lap joint: spot (25.4 x 90 x 12.7); continuous (240 x 90 x 12.7)	322.6, (67)	CF/PEEK, PEEK mesh ED	Spot: 450-600 ms (optimum 550 ms); continuous: 25-35 mm/s (optimum 25 mm/s); f: 20 kHz; A: 80 µm; F: 800 N	Ultrasonic welding	Frictional, viscoelastic heating, melting of mesh ED, consolidation	40.3 (Spot), 33.9 (Continuous)
[17]	Single-lap joint (101.6 x 25.4 x 1.85)	323, (50)	CF/PPS (thermoplastic composite), PPS mesh energy director	f: 20 kHz; F: 500 N; A: 70 µm; d: 0.12 mm	Ultrasonic welding	Frictional, viscoelastic heating, melting of mesh ED, consolidation	32.6
[18]	Single-lap joint (70 x 60 x 2)	1400, (30)	CF/PA66 (thermoplastic composite)	f: 20 kHz; A: 80 µm; P: 2 MPa; v: 10-20 mm/s	Continuous ultrasonic welding	Friction, viscoelastic heating, fusion bonding	15.72

3. EXPERIMENTAL MECHANICAL ASSESSMENT OF BONDED JOINTS BETWEEN GFRP REBARS

3.1. Materials

The experimental programme involved the development and mechanical assessment of bonded joints between GFRP rebars, with particular attention given to the influence of rebar diameter and adhesive material on joining behaviour. The specimens were therefore produced using two principal material groups: (i) braided GFRP rebars, which constituted the adherends, and (ii) adhesives used to form the connections between intersecting rebars. Two nominal rebar diameters, 4 mm and 10 mm, were considered, while different adhesive systems were investigated to evaluate their suitability for the proposed joining configuration. The constituent materials, relevant physical and mechanical properties, and characteristics of the GFRP rebars and adhesives are presented in the following sections.

3.1.1. GFRP Rebars

The glass fibre-reinforced polymer (GFRP) rebars investigated in this study were produced and supplied by The Light Rebar Company (LRC), Guimarães, Portugal. The reinforcement is manufactured as a braided composite rebar consisting of a continuous E-glass-fibre-reinforced core embedded in a thermosetting epoxy matrix and an externally braided surface. The external architecture incorporates a braided layer together with an additional helically arranged cord, producing the characteristic textured surface of the reinforcement. This configuration is intended to improve mechanical interlocking and bond with the surrounding material, while the outer helical cord provides additional resistance to shear transfer.

The reinforcing phase of the composite consists of continuous ECR-glass fibres produced by a direct-draw process. The glass rovings are treated with a silane-based sizing system compatible with thermosetting polymer matrices, including epoxy resins. The rovings are

designed to provide rapid resin wet-out, uniform tension during processing and resistance to fibre damage, fuzz formation and entanglement. These characteristics facilitate consistent fibre impregnation and alignment during continuous composite manufacturing. According to the technical data provided by the supplier, the impregnated glass strands exhibit a tensile strength exceeding 1600 MPa, while a rod bending strength greater than 650 MPa is reported [19].

The glass fibres are embedded within a thermosetting Westlake epoxy matrix consisting of a low-viscosity liquid epoxy resin combined with an accelerated anhydride curing agent. The system is intended for composite manufacturing processes including pultrusion and filament winding. Its low viscosity facilitates fibre impregnation during manufacturing, while the cured matrix binds the individual fibres, transfers stresses between them and provides protection to the reinforcing phase. The resin system is additionally characterised by low moisture absorption and good thermal deformation resistance. For the cured, non-reinforced resin system, the manufacturer reports a tensile strength of 142 ± 10 MPa, a tensile modulus of 3150 ± 100 MPa and an elongation at break of 7.6 ± 2%. The corresponding flexural strength and flexural modulus are 86 ± 10 MPa and 3180 ± 150 MPa, respectively. Differential scanning calorimetry indicates a glass-transition onset temperature of 117 ± 3 °C and a midpoint temperature of 122 ± 3 °C [20].

The resulting reinforcement comprises a glass-fibre-reinforced epoxy core surrounded by a polyester braided surface layer. An additional outer helical braiding cord further modifies the surface profile of the rebar. As illustrated schematically in the manufacturer's technical documentation, the longitudinal reinforcement fibres form the principal resistant core, while the impregnated braided outer fibres form the external layer shown in Figure 3-1. This arrangement creates a heterogeneous composite architecture in which the continuous fibres primarily govern the longitudinal response, while the matrix, fibre–matrix interaction and external braiding contribute to transverse behaviour, shear resistance and interfacial load transfer.

According to the manufacturer's technical characterisation, the finished braided GFRP reinforcement has a characteristic tensile strength greater than 1200 MPa and a longitudinal

elastic modulus greater than 50 GPa, with a tensile elongation exceeding 2.40%. The reported transverse shear strength exceeds 164 MPa, while the interlaminar shear strength exceeds 62.5 MPa. A glass transition temperature of approximately 120 °C and a maximum service temperature of 88.2 °C are reported. The nominal density of the reinforcement is approximately 2.0 ± 0.4 g/cm³ [21].

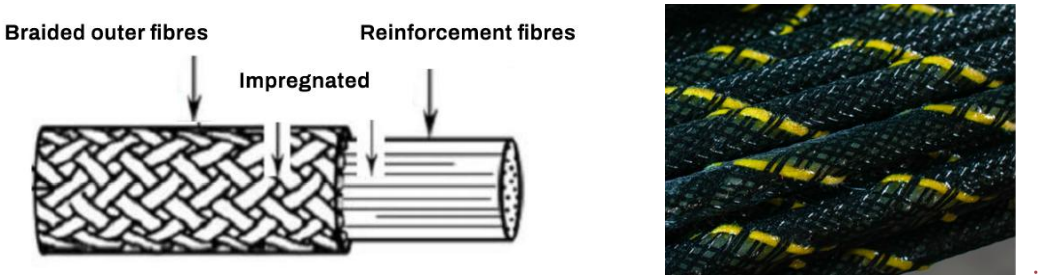


Figure 3-1 Schematic diagram of GFRP braided rebars (Courtesy of The Light Rebar Company)

Although the reinforcement is manufactured in several nominal diameters, only the 4 mm and 10 mm rebars were considered in the present Dissertation. The nominal diameter indicated by the manufacturer refers to the resistant composite core formed by the glass fibres and polymer matrix rather than the maximum external dimension of the braided rebar. The external strand therefore results in a local increase in the overall diameter beyond the stated nominal value. This distinction is relevant to the present investigation because the external surface geometry directly affects the dimensions and contact conditions of the bonded joints. The 4 mm rebar has a nominal mass per unit length of 28.7 g/m and is identified by a blue outer cord, whereas the 10 mm rebar has a nominal mass per unit length of 164.6 g/m and is identified by a yellow cord (see Figure 3-2). Despite being manufactured from the same constituent material system and having the same general braided architecture, the two diameters differ considerably in cross-sectional dimensions and external surface geometry. Both diameters were therefore investigated independently within the experimental programme to evaluate the influence of rebar size on the behaviour of the developed joints.



Figure 3-2 Bundles of 4 mm & 10 mm GFRP rebars (courtesy of The Light Rebar Company)

3.1.2. Adhesives

The selection of the joining material was a central aspect of the experimental programme, as the performance of the GFRP grid intersections depends on the ability of the joint to transfer forces between two orthogonally positioned rebars while maintaining sufficient stiffness and integrity. Unlike conventional bonded lap joints, the geometry investigated in this study involves two curved rebar surfaces and a relatively localised bonding region. The joining material must therefore combine adequate adhesion to the GFRP surface with suitable shear resistance, stiffness and deformation capacity. At the same time, the proposed grid system is intended for an automated manufacturing process; consequently, processing characteristics such as working time, development of handling strength, dispensing requirements and the need for surface preparation were also considered important in the selection of the materials. Eight joining materials were considered and are hereafter designated Adhesive 1 to Adhesive 8. This designation is maintained throughout the experimental programme to provide a consistent identification of the materials. Table 3-1 provides a summary of the main physical, mechanical and processing properties of the joining materials, according to the manufacturers' technical datasheets.

Adhesives 1 and 2 were supplied by 3M, Adhesives 3–6 by Plexus, Adhesive 7 by Westlake, while Adhesive 8 was a thermoplastic joining material by CENTI. The investigated systems therefore covered different material chemistries and mechanical responses, ranging from relatively stiff structural adhesives to more deformable systems, together with a thermoplastic alternative. Adhesives 1 and 2 are acrylic-based systems, Adhesives 3–6 are two-component methacrylate structural adhesives, and Adhesive 7 is an epoxy-based bonding paste developed for composite applications.

The mechanical characteristics of the candidate materials varied considerably. Among the Plexus systems, the reported tensile moduli ranged from approximately 0.56–0.75 GPa for Adhesive 5 to 1.52–2.06 GPa for Adhesive 3. Their elongation at break also ranged from 5–11% for Adhesive 6 to 35–65% for Adhesive 5, illustrating the substantially different levels of stiffness and deformability represented within the experimental programme. These differences were considered particularly relevant for the rebar intersections because a comparatively stiff adhesive may favour efficient force transfer but may also concentrate

stresses within the localised bonded region, whereas a more deformable adhesive can accommodate greater relative movement between the intersecting rebars.

Compatibility with composite substrates was another important consideration. The technical datasheets do not employ identical substrates or test configurations and therefore cannot be compared as if the reported lap-shear strengths represented an intrinsic material property. Nevertheless, several manufacturers provide results directly involving fibre-reinforced polymers. Adhesive 1 was identified as suitable for FRP as a secondary bonding substrate and exhibited substantial overlap shear resistance on the tested FRP substrate. Adhesive 2 achieved a reported overlap shear strength of 19.2 MPa on fibre-reinforced plastic following abrasion and solvent cleaning. Among the Plexus materials, Adhesive 4 was tested on PU-GFRP and Adhesive 6 on FRP, with reported lap-shear strengths of 3.4 and 16.5 MPa, respectively. Adhesive 7 was tested directly on GFK/GFRP substrates, for which lap-shear strengths between 22.8 and 32.4 MPa were obtained depending on the curing condition. These values provided useful preliminary indications of compatibility with composite substrates but were not used as direct predictions of the strength of the rebar joints investigated experimentally.

Processing behaviour was equally important because the eventual manufacturing concept requires adhesive deposition and positioning to be integrated into a repeatable production sequence. The candidate systems presented markedly different working windows. Adhesive 1 provides only approximately 2.5–3 min of work life at 23 °C and requires considerably longer to develop handling strength, whereas Adhesive 2 provides an open time of approximately 10 min and develops handling strength in approximately 20 min. Adhesives 3–6 generally provide working times of approximately 3–6 min at room temperature and develop initial shear resistance within a relatively short period, while their technical documentation also permits cartridge or automated meter/mix/dispense application. Adhesive 7 provides a longer working time of approximately 10–15 min and is supplied as a cartridge system with static mixing.

Surface preparation requirements also differed between the materials. For Adhesive 2, the recommended preparation of composite substrates consists of cleaning, light abrasion and

subsequent solvent cleaning. The Plexus systems generally require little surface preparation provided that the bonding region is free from grease, dirt and other contaminants; light abrasion may nevertheless be applied to composite surfaces to remove mould-release residues or increase the available surface area. Adhesive 7 similarly requires the surfaces to be dry and free from grease without prescribing extensive preparation. Minimising such operations is particularly relevant to automated grid production, since additional cleaning, abrasion or chemical treatment stages would increase the complexity and duration of the manufacturing sequence.

Adhesive 8 was included to examine a fundamentally different joining approach based on thermoplastic behaviour. In contrast to the thermosetting systems, which develop their final properties through an irreversible curing reaction, a thermoplastic material can be softened by heating and subsequently solidified by cooling. Its inclusion therefore allowed the potential of a rapid joining process with no conventional chemical curing period to be explored. Since no manufacturer technical datasheet containing material-specific mechanical properties was available for Adhesive 8, numerical values for its modulus, strength or durability are not assigned in the following comparison; these characteristics are considered through the experimental response of the joints.

Table 3-1 Summary of the main physical, mechanical and processing properties of the joining materials, according to the manufacturers' technical datasheets.

Material	Manufacturer / type	Mix ratio (vol.)	Work time (min)	Handling time (min)	Full cure time (hrs)	Tensile strength (MPa)/ (Elongation)(%)	FRP/GFRP shear strength & relevant characteristics
Adhesive 1	3M / Acrylic	10:1	2.5–3	120-180	24	11.7–13.0 / (4.5–5.3)	16.9–17.1 MPa on FRP; short working window; cartridge dispensing
Adhesive 2	3M / Acrylic	10:1	10	20	24	16.7 / (79)	19.2 MPa on FRP; abrasion and cleaning recommended
Adhesive 3	Plexus / Methacrylate	1:1	3–6	10-13	72	24.2–29.6 / (20–40)	N/S on FRP; 0.25–3.2 mm gap tolerance; suitable for automated dispensing
Adhesive 4	Plexus / Methacrylate	10:1	4–6	15-17	24	16.8–20.5 / (20–40)	3.4 MPa on PU-GFRP; 0.75–9.5 mm gap tolerance; composite-oriented
Adhesive 5	Plexus / Methacrylate	10:1	3–6	7-8	24	12.1–14.8 / (35–65)	N/S on FRP; relatively compliant; 1–4 mm gap tolerance; rapid setting
Adhesive 6	Plexus / Methacrylate	1:1	3–6	12-14	72	24.1–26.2 / (5–11)	16.5 MPa on FRP; little/no surface preparation
Adhesive 7	Westlake / Epoxy	10:1	10–15	N/S	24	N/S	22.8–32.4 MPa on GFRP; composite bonding; static mixing
Adhesive 8	CENTI/ Thermoplastic hot-melt pellets	—	—	Rapid cooling	—	N/S	N/S; heat-activated joining; no conventional thermoset curing period

Durability was also considered in the assessment of the joining materials, particularly because the proposed GFRP grid system may be exposed to variations in temperature, moisture and chemically aggressive environments during service. Table 3-2 provides a summary of the durability and environmental resistance characteristics of the joining materials, as reported in the manufacturers' technical datasheets.

The available manufacturer data indicate different levels of environmental resistance, although direct comparison between the adhesives should be made cautiously because the reported conditioning procedures, substrates and exposure durations were not identical. Adhesive 1 (3M) showed good resistance to water, humidity and several chemical environments. Following 14 days of exposure, bonded HDPE specimens retained relatively high overlap shear resistance after water, salt-water, sodium hydroxide, hydrochloric acid, isopropyl alcohol, antifreeze and diesel exposure, whereas substantially greater reductions occurred following exposure to gasoline, toluene and acetone. Its strength was also temperature-dependent; on the tested FRP substrate, the overlap shear strength decreased progressively as the test temperature increased from 23 °C to 82 °C. Adhesive 2 (3M) was similarly characterised for environmental exposure, retaining 68% and 73% of its reference overlap shear performance after 500 h immersion in water and salt water, respectively, and 52% following exposure to 85 °C and 85% relative humidity. Diesel exposure resulted in 96% retention, whereas gasoline was considerably more detrimental, with only 19% retained performance. Its strength also decreased with increasing temperature, retaining 51% at 49 °C and 38% at 82 °C relative to the room-temperature reference.

For Adhesives 3–6 (Plexus), the technical datasheets indicate resistance to hydrocarbons, salt solutions, and acids and bases within approximately pH 3–10, while identifying strong polar solvents and strong acids or bases as potentially detrimental. Their temperature-strength retention curves further show that bond performance generally decreases as temperature increases, although the extent of the reduction varies between formulations. Adhesive 5 is additionally described as retaining high toughness at temperatures below −17 °C, indicating comparatively favourable low-temperature behaviour. Adhesive 6 is reported to withstand continuous temperatures up to 121 °C without degradation and was also evaluated after 1000 h salt-fog exposure, providing additional evidence of resistance to prolonged environmental

conditioning. Adhesive 7 (Westlake) has a stated operational temperature range of −40 °C to +70 °C after post-curing and an ultimate glass-transition temperature above 80 °C; however, its technical datasheet does not provide equivalent long-term water, humidity, salt-spray or chemical-retention data, preventing a quantitative environmental comparison with the other systems. For Adhesive 8 (CENTI), no material-specific technical datasheet or environmental ageing results were available; therefore, its durability cannot be quantified from manufacturer data and would require experimental evaluation under representative service conditions.

Table 3-2 Summary of the durability and environmental resistance characteristics of the joining materials, as reported in the manufacturers' technical datasheets.

Material	Main durability information available from TDS
Adhesive 1 – 3M	14-day water, humidity, salt water and chemical exposure; temperature-dependent FRP strength up to 82 °C
Adhesive 2 – 3M	500 h water, salt water, fuels and humidity exposure; elevated-temperature strength retention
Adhesive 3 – Plexus	Hydrocarbon, salt, acid/base resistance; temperature-strength retention
Adhesive 4 – Plexus	Hydrocarbon, salt, acid/base resistance; temperature-strength retention
Adhesive 5 – Plexus	Hydrocarbon, salt, acid/base resistance; temperature-strength retention; enhanced toughness below −17 °C
Adhesive 6 – Plexus	Chemical resistance; temperature-strength retention; 1000 h salt-fog result; continuous temperature capability to 121 °C
Adhesive 7 – Westlake	Operational range −40 to +70 °C after post-cure; Tg >80 °C; no comparable environmental ageing programme reported
Adhesive 8 – CENTI Thermoplastic pellets	No material-specific durability data available

3.2. Test Setup and Programme

3.2.1. Specimen Configuration and Preparation

The mechanical performance of the bonded GFRP intersections was evaluated through tensile testing of individual cross-joint specimens. Each specimen consisted of two GFRP rebars positioned orthogonally and connected at a single intersection using one of the joining materials described in Section 3.1.2. Testing an individual intersection allowed the load-transfer behaviour of the joint to be isolated from the response of a complete grid and provided a consistent configuration for comparing the different joining materials and rebar diameters. The configuration adopted was inspired in the EN ISO 15630-2:2002 [22] (Steel for the reinforcement and prestressing of concrete — Test methods — Part 2: Welded fabric) since, to the best knowledge of this work, there is no standard applied to FRP rebars.

The geometry adopted for the specimens is presented in Figure 3-3. The vertical rebar extended 250 mm above the intersection and 80 mm below it, while the horizontal rebar extended 100 mm on either side of the joint, giving a total horizontal length of 200 mm. The same general configuration was maintained for the specimens manufactured using 4 mm and 10 mm diameter rebars.

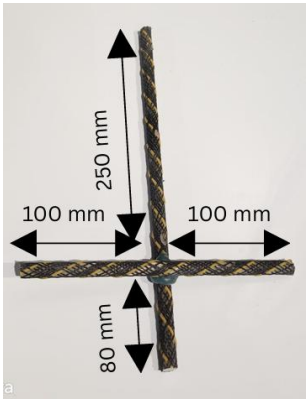


Figure 3-3 Geometry and dimensions of the single-joint GFRP specimen used in the experimental programme.

The specimens were tested using an MTS Exceed E45.105 universal testing machine (UTM), with a maximum capacity of 100 kN. A purpose-adapted steel fixture was employed to restrain the horizontal rebar while the vertical rebar was subjected to tensile loading. As shown in

Figure 3-4, the horizontal member was supported by the upper surface of the fixture on both sides of the intersection, while the upper end of the vertical rebar was gripped by the testing machine. The displacement of the specimens during tensile testing was measured using a video extensometer. Prior to testing, two contrasting reference dots were applied using white correction fluid (Blanco): one at the rebar intersection and the second on the vertical rebar. The video extensometer camera was positioned in front of the specimen and calibrated before the test. As tensile loading was applied to the vertical rebar, the relative movement between the two reference points was continuously tracked by the camera. The resulting displacement data were recorded together with the corresponding applied force, allowing the force–displacement response of each specimen to be obtained.

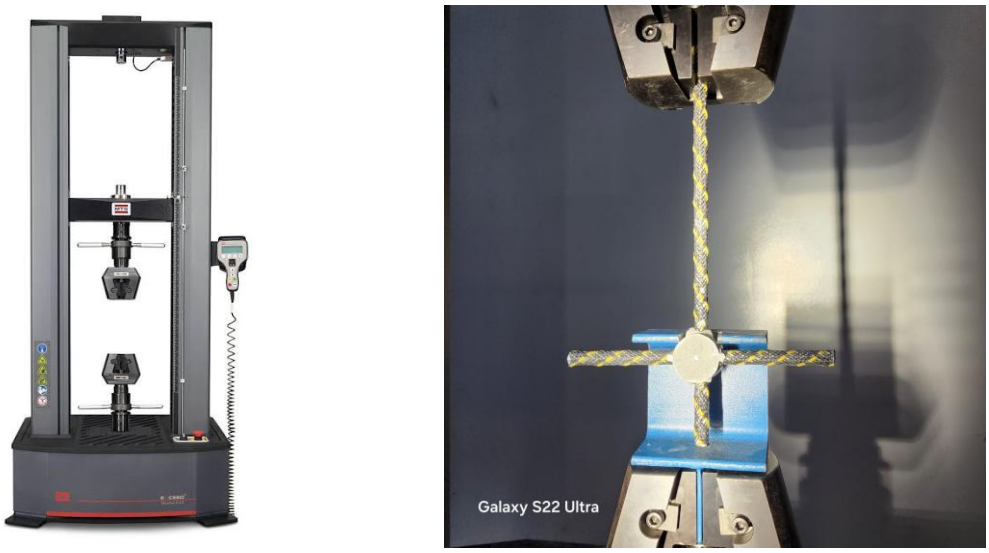


Figure 3-4 MTS tensile testing arrangement and fixture used for the single-joint GFRP specimens.

All specimens were tested under displacement-controlled loading at a constant crosshead velocity of 1 mm/min. The applied force was continuously recorded by the load cell of testing system, while an extensometer with a gauge length of 25 mm was used to measure the deformation of the loaded rebar. Testing was generally continued until joint failure, identified by the loss of load-carrying capacity and a reduction in the recorded force towards zero. In tests where substantial additional displacement produced no further meaningful change in the recorded force after the principal joint response had occurred, the test was manually terminated to avoid unnecessary continuation of the loading cycle.

The slip associated with the joint was determined by correcting the measured displacement for the elastic elongation of the GFRP rebar. This correction was necessary because the measured deformation contains not only relative movement at the bonded intersection but also the elastic deformation of the loaded rebar over the measured length. The elastic elongation of the GFRP rebar was calculated according to:

$$\delta_e = \frac{Fl}{EA} \tag{3.1}$$

and the corresponding joint slip was obtained as:

$$s = \delta - \frac{Fl}{EA} \tag{3.2}$$

where s is the corrected joint slip (in mm), δ is the measured displacement obtained from the UTM (in mm), F is the instantaneous applied force (in N), l is the extensometer gauge length (25 mm), E is the longitudinal elastic modulus of the GFRP rebar (50 GPa), and A is the cross-sectional area of the corresponding rebar (in mm²). The elastic modulus was adopted from the manufacturer's reported longitudinal modulus for the GFRP reinforcement. For consistency in the displacement correction, a value of 50 GPa was used for both rebar diameters.

The nominal cross-sectional area was determined from the corresponding rebar diameter according to:

$$A = \frac{\pi d^2}{4} \tag{3.3}$$

resulting in nominal cross-sectional areas of 12.57 mm² and 78.54 mm² for the 4 mm and 10 mm rebars, respectively. The correction was applied to the recorded data throughout the loading history, thereby allowing the force–slip response of each joint to be established independently of the elastic elongation associated with the measured portion of the GFRP rebar.

For each joining material and rebar diameter, three nominally identical specimens were tested. The maximum force, corresponding slip and calculated shear strength were subsequently determined for each specimen. Following testing, the joints were visually inspected to identify the governing failure mode and any relevant features associated with

damage to the adhesive, GFRP surface or rebar. These measurements and observations formed the basis for the comparison of the different joining systems presented in Section 3.3.

3.2.2. Experimental Programme

The experimental programme was designed to assess the mechanical response of the eight joining materials when applied to the two GFRP rebar diameters considered in this study. For each joining material, three nominally identical single-joint specimens were prepared and tested for both the 4 mm and 10 mm rebars. This resulted in 16 test series and a total of 48 specimens. The complete experimental programme is summarised in Table 3-3.

Table 3-3 Experimental programme for the mechanical testing of the GFRP single-joint specimens.

Test series	Joining material	Manufacturer / type	Rebar diameter (mm)	No. of specimens
A1-4	Adhesive 1	3M / Acrylic	4	3
A1-10	Adhesive 1	3M / Acrylic	10	3
A2-4	Adhesive 2	3M / Acrylic	4	3
A2-10	Adhesive 2	3M / Acrylic	10	3
A3-4	Adhesive 3	Plexus / Methacrylate	4	3
A3-10	Adhesive 3	Plexus / Methacrylate	10	3
A4-4	Adhesive 4	Plexus / Methacrylate	4	3
A4-10	Adhesive 4	Plexus / Methacrylate	10	3
A5-4	Adhesive 5	Plexus / Methacrylate	4	3
A5-10	Adhesive 5	Plexus / Methacrylate	10	3
A6-4	Adhesive 6	Plexus / Methacrylate	4	3
A6-10	Adhesive 6	Plexus / Methacrylate	10	3
A7-4	Adhesive 7	Westlake / Epoxy	4	3
A7-10	Adhesive 7	Westlake / Epoxy	10	3
A8-4	Adhesive 8	CENTI / Thermoplastic hot-melt pellets	4	3
A8-10	Adhesive 8	CENTI / Thermoplastic hot-melt pellets	10	3
			Total	48

For each test series, the force–slip response was recorded and the maximum force, corresponding slip and shear strength were determined. The three specimens within each series were subsequently used to determine the average response and coefficient of variation (CoV). Following testing, the failure mode and relevant observations for each joint were also documented. A CoV greater than 20% was considered to indicate significant dispersion between the specimens of a given series, in accordance with the assessment approach established for the experimental programme.

3.3. Results and Discussion

The experimental results obtained from the single-joint tests are presented and discussed in this section with the aim of assessing the effectiveness of the different joining materials and the influence of rebar diameter on joint performance. The response of each test series was evaluated in terms of force–slip behaviour, maximum force, slip at maximum force, shear strength and observed failure mode. The three specimens tested for each condition were considered collectively to assess both the representative response and the variability within each series. The results are first examined through the force–slip response of the individual specimens, followed by a comparative assessment of the principal mechanical parameters and, finally, an analysis of the observed failure mechanisms.

3.3.1. Force–Slip Behaviour and Key Mechanical Results

This section examines the behaviour of all eight joining materials through their force–slip curves, together with the maximum force, corresponding slip and nominal shear strength attained by each joint configuration.

The mechanical response of the joints produced with Adhesive 1 is presented in Figure 3-5. For the 4 mm rebars, the maximum force ranged from 0.17 to 0.22 kN, with corresponding slip values of 2.04 – 3.72 mm and nominal shear strengths of 14 – 18 MPa. The three specimens therefore exhibited relatively comparable load capacities, although Specimen 2 showed a noticeably larger slip. For the 10 mm rebars, a greater variation was observed, with maximum forces ranging from 0.19 to 0.50 kN and nominal shear strengths from 2.4 to 6.4

MPa; the highest response was obtained for Specimen 3, reaching 0.50 kN at a slip of 2.16 mm. Although the 10 mm specimens generally developed higher absolute forces, their nominal shear strengths were considerably lower than those of the 4 mm specimens. The force–slip curves further show a gradual post-peak reduction in load rather than an abrupt loss of capacity, indicating progressive degradation of the joint with increasing slip.

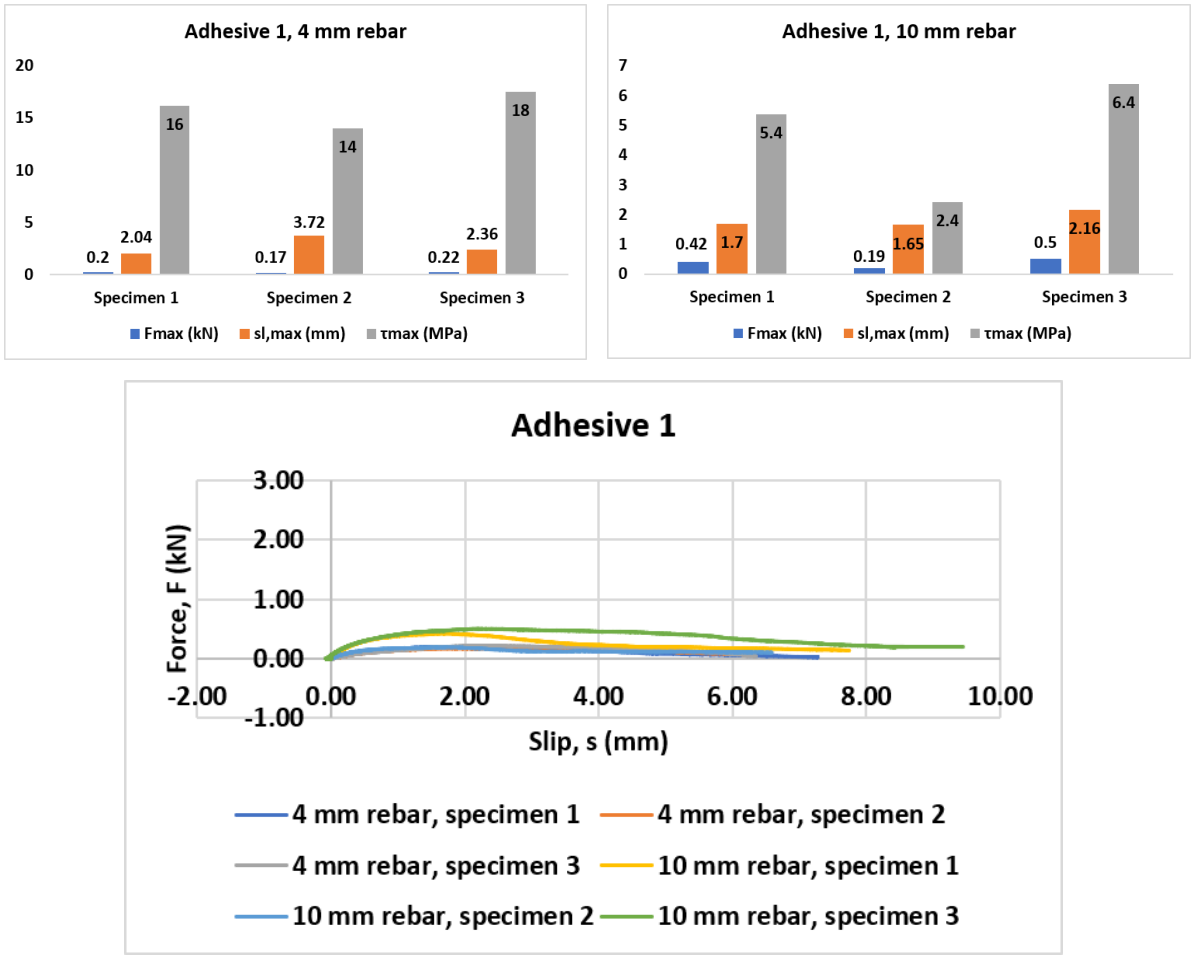


Figure 3-5 Force–slip response and joint performance of Adhesive 1 for 4 mm and 10 mm rebars.

For Adhesive 2 in Figure 3-6, the 4 mm specimens exhibited maximum forces between 0.22 and 0.29 kN, corresponding to nominal shear strengths of 17.7 – 23.0 MPa, with relatively small slips of 0.59 – 0.96 mm. Specimen 1 achieved the highest response within this series, reaching 0.29 kN and 23.0 MPa at a slip of 0.96 mm. A markedly greater variation was observed for the 10 mm rebars, where the maximum force ranged from 0.12 to 1.03 kN and the corresponding nominal shear strength from 1.5 to 13.2 MPa. Specimen 3 clearly exhibited the highest performance, attaining 1.03 kN and 13.2 MPa at 0.90 mm slip, while Specimen 2

showed substantially lower capacity. The force–slip curves reflect this dispersion within the 10 mm series, particularly the distinctly higher response of Specimen 3, while the 4 mm specimens displayed a more closely grouped and consistent behaviour.

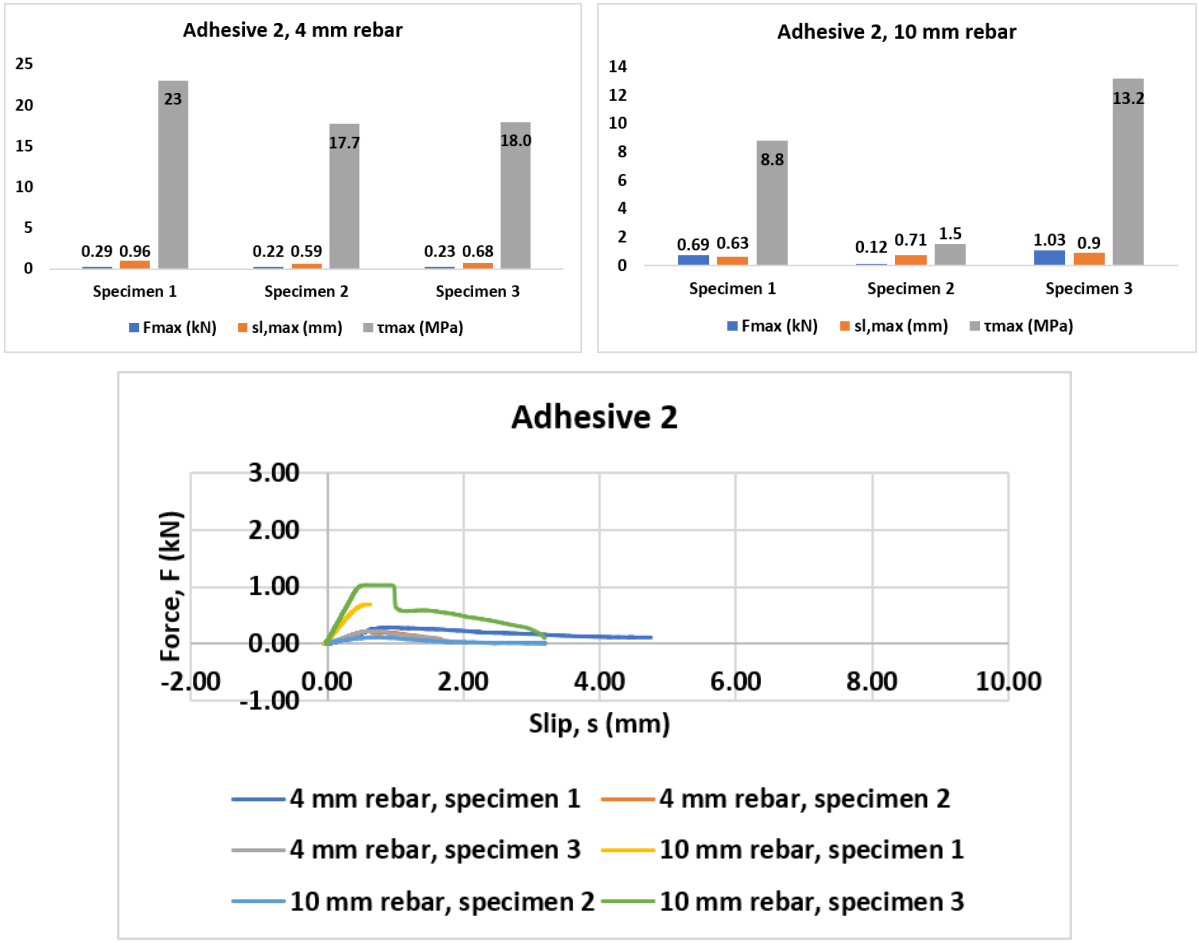


Figure 3-6 Force–slip response and joint performance of Adhesive 2 for 4 mm and 10 mm rebars.

As shown in Figure 3-7, Adhesive 3 exhibited relatively high joint capacities for the 4 mm rebars, with maximum forces ranging from 0.32 to 0.58 kN and corresponding nominal shear strengths of 25.6 – 46.4 MPa. Specimen 1 achieved the highest response, reaching 0.58 kN and 46.4 MPa at a slip of 0.80 mm, closely followed by Specimen 2 with 0.57 kN and 45.5 MPa at 0.97 mm, while Specimen 3 showed a lower capacity of 0.32 kN. For the 10 mm rebars, the maximum force ranged from 0.31 to 0.76 kN, corresponding to nominal shear strengths of 4.0 – 9.7 MPa, with Specimen 2 attaining the highest force of 0.76 kN at a comparatively larger slip of 1.96 mm. The force–slip curves in Figure 3-7 further show a broader post-peak response for some specimens, particularly the higher-capacity 10 mm specimen, while the 4 mm joints

consistently developed considerably higher nominal shear strengths despite the higher absolute force attained by one of the 10 mm specimens.

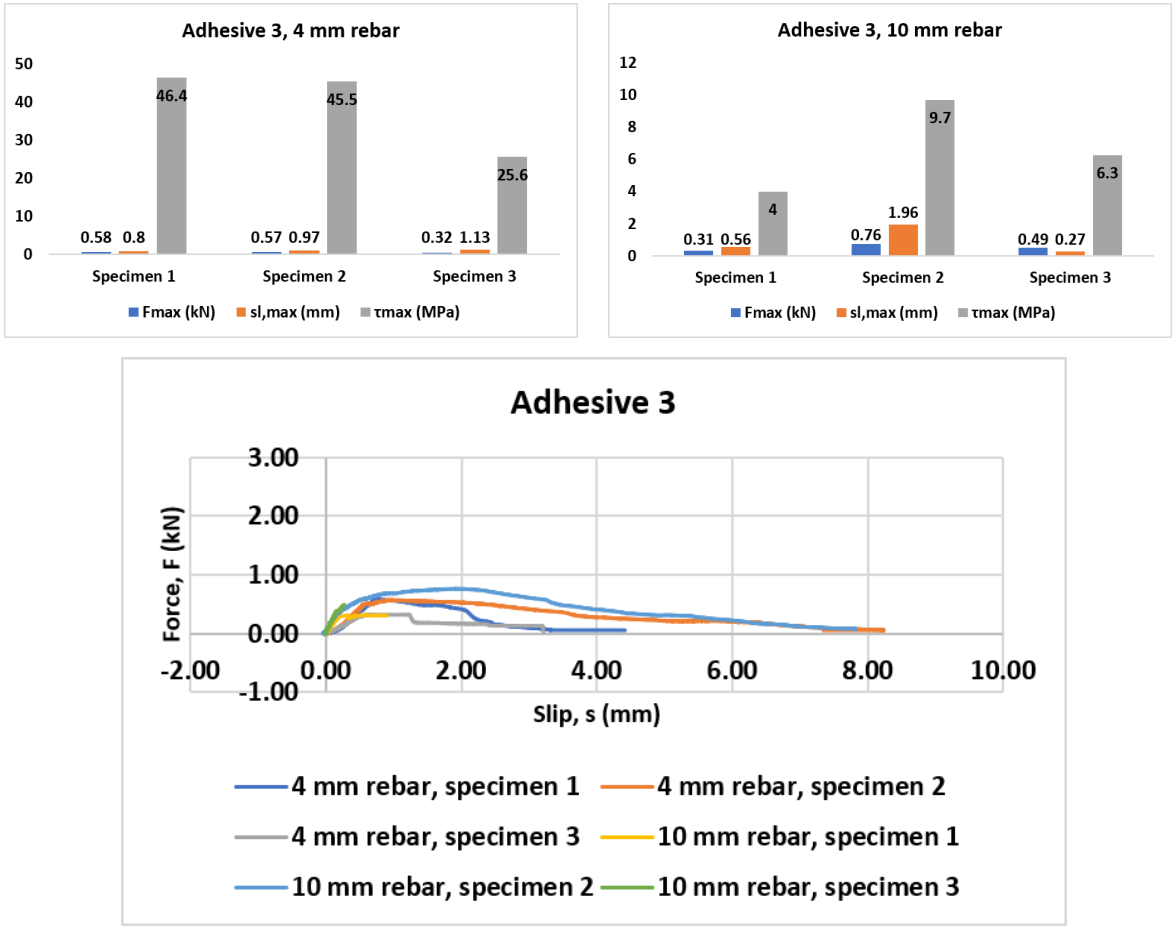


Figure 3-7 Force–slip response and joint performance of Adhesive 3 for 4 mm and 10 mm rebars.

As shown in Figure 3-8, Adhesive 4 exhibited maximum forces of 0.38 – 0.52 kN for the 4 mm rebars, corresponding to nominal shear strengths of 29.9 – 41.2 MPa at slips between 1.47 and 1.74 mm. Specimen 2 achieved the highest response within this series, reaching 0.52 kN and 41.2 MPa at a slip of 1.74 mm. The 10 mm specimens developed substantially higher absolute forces, ranging from 0.83 to 1.79 kN, with corresponding nominal shear strengths of 10.5 – 22.8 MPa; Specimen 3 showed the highest overall force of 1.79 kN and a shear strength of 22.8 MPa at 1.75 mm slip. The force–slip curves in Figure 3-8 also reveal a more extended post-peak response for the 10 mm joints, particularly Specimen 3, which retained considerable load over a larger slip range before progressively losing its capacity. Overall, the 10 mm joints carried considerably greater absolute forces, whereas the 4 mm joints attained higher nominal shear strengths.

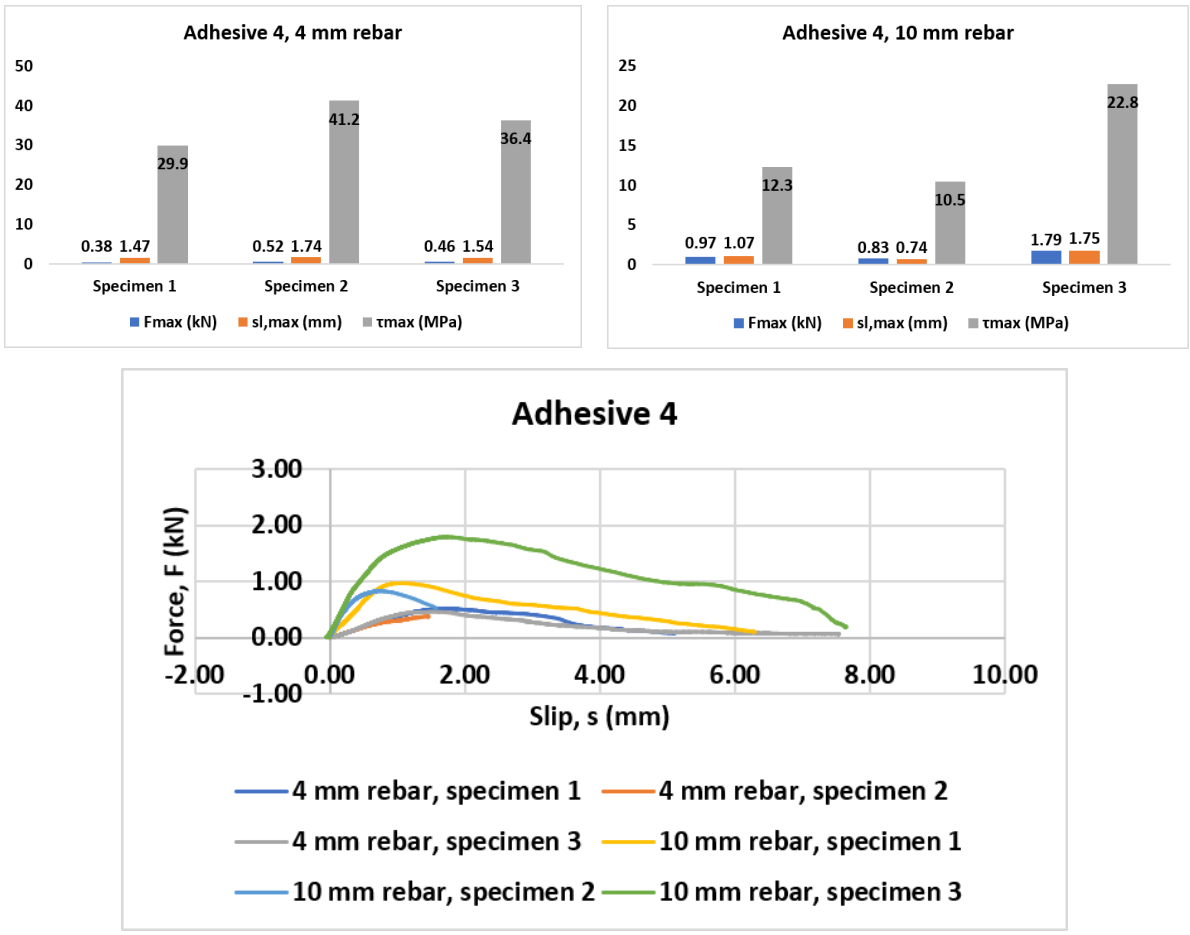


Figure 3-8 Force–slip response and joint performance of Adhesive 4 for 4 mm and 10 mm rebars.

As shown in Figure 3-9, Adhesive 5 exhibited maximum forces between 0.23 and 0.41 kN for the 4 mm rebars, corresponding to nominal shear strengths of 18.6 – 32.9 MPa at slips ranging from 0.54 to 1.19 mm. Specimen 2 achieved the highest response within this series, reaching 0.41 kN and 32.9 MPa at a relatively small slip of 0.54 mm. In contrast, the 10 mm specimens developed considerably higher maximum forces of 0.85 – 1.53 kN, corresponding to nominal shear strengths of 10.8 – 19.4 MPa, with Specimen 1 attaining the highest force of 1.53 kN and shear strength of 19.4 MPa at 1.84 mm slip. The force–slip curves in Figure 3-9 show a distinctly broader response for the 10 mm joints, which continued to transfer load over substantially larger slip ranges after reaching their maximum force, particularly Specimen 2. Thus, while the 10 mm joints demonstrated greater absolute load-carrying capacity and more extended post-peak behaviour, the 4 mm joints again developed higher nominal shear strengths.

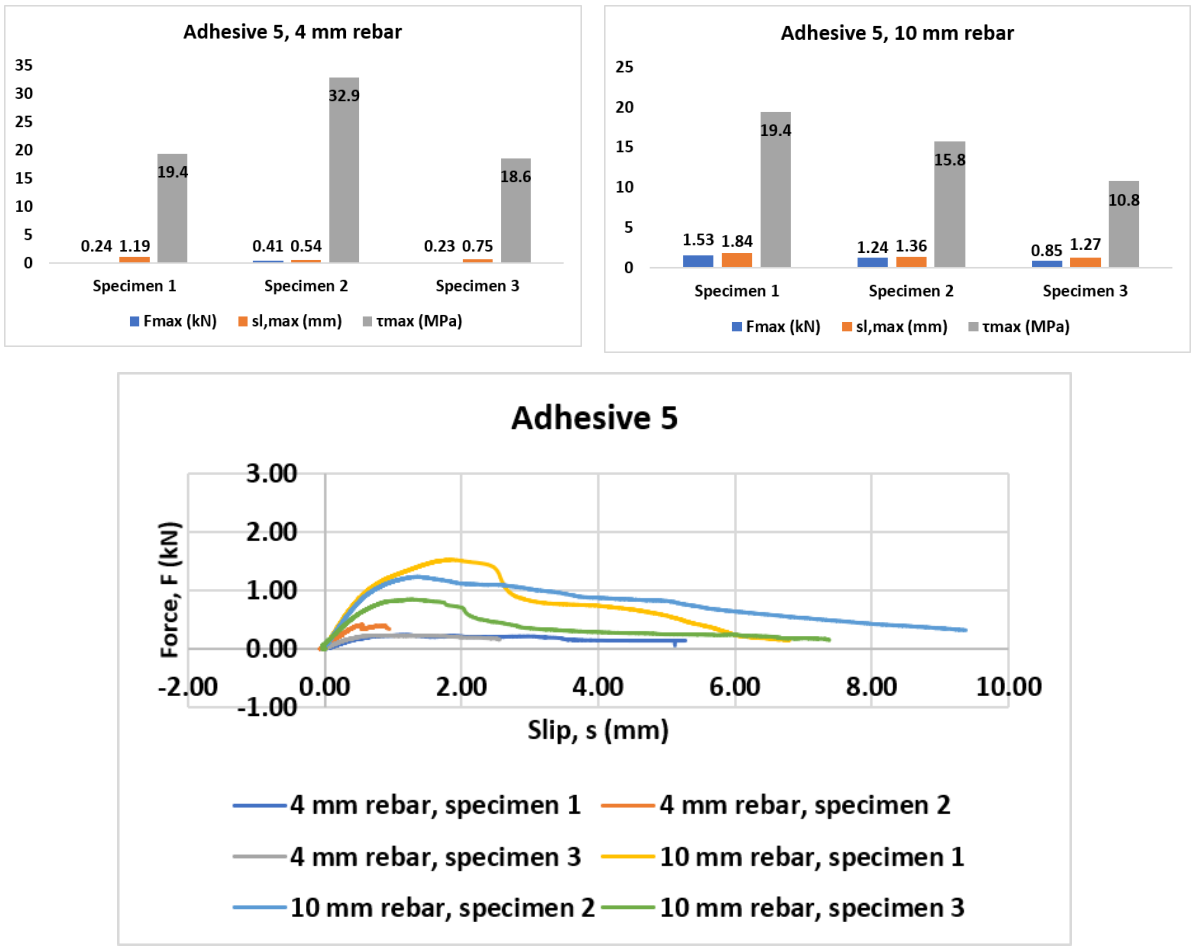


Figure 3-9 Force–slip response and joint performance of Adhesive 5 for 4 mm and 10 mm rebars.

As shown in Figure 3-10, Adhesive 6 exhibited maximum forces of 0.42 – 0.56 kN for the 4 mm rebars, corresponding to nominal shear strengths of 33.3 – 45.1 MPa, with slips ranging from 0.66 to 2.35 mm. Specimen 2 achieved the highest response within this series, reaching 0.56 kN and 45.1 MPa at a slip of 0.66 mm, while Specimen 3 exhibited the largest slip of 2.35 mm. For the 10 mm rebars, substantially higher maximum forces of 1.06 – 2.19 kN were obtained, corresponding to nominal shear strengths of 13.5 – 27.9 MPa; Specimen 2 showed the highest overall performance, attaining 2.19 kN and 27.9 MPa at a slip of 0.99 mm. The force–slip curves in Figure 3-10 show a relatively rapid development of load for the 10 mm specimens, particularly Specimen 2, whereas greater variation in deformation behaviour was evident among the 4 mm specimens. Overall, Adhesive 6 provided considerably greater absolute load capacity for the 10 mm joints, while the 4 mm joints continued to exhibit higher nominal shear strengths.

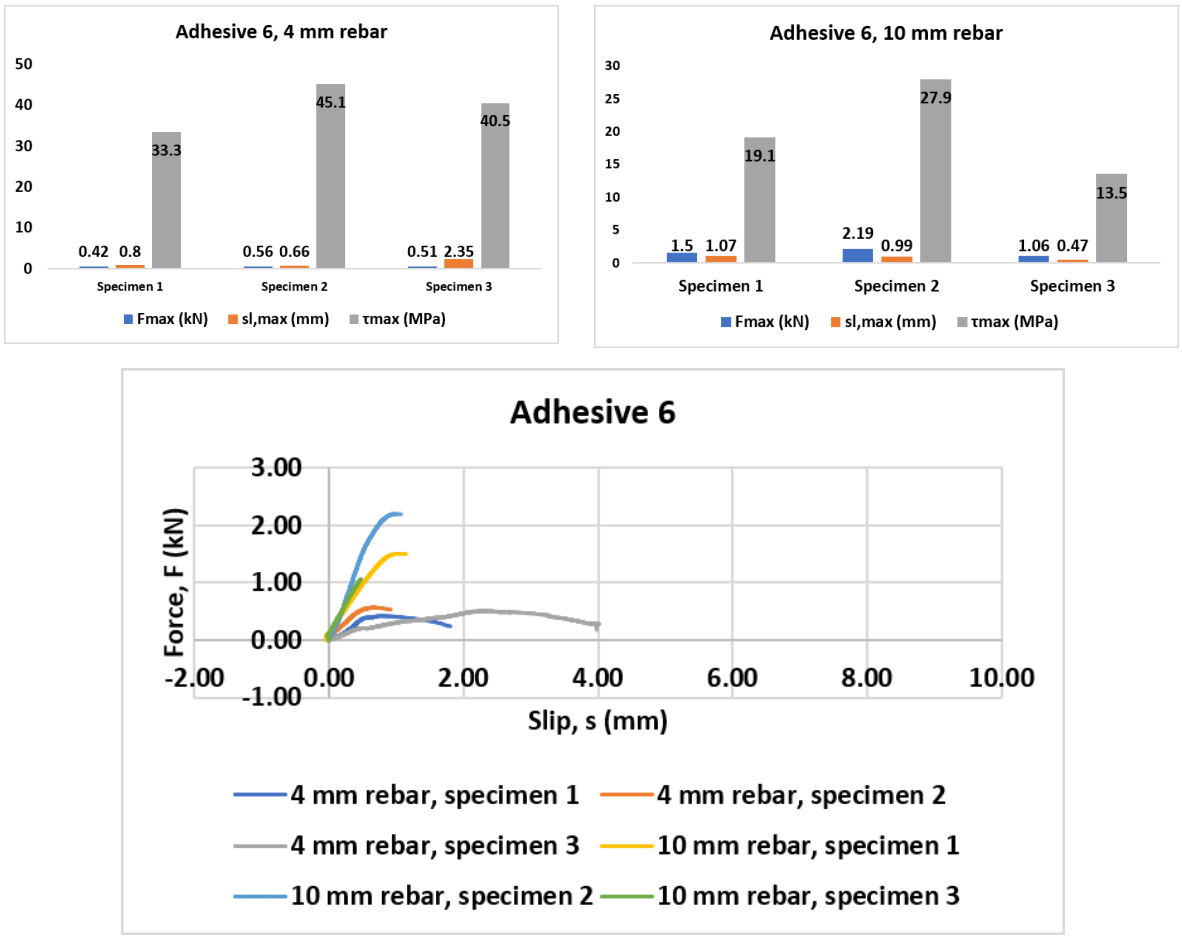


Figure 3-10 Force–slip response and joint performance of Adhesive 6 for 4 mm and 10 mm rebars.

As shown in Figure 3-11, Adhesive 7 exhibited maximum forces between 0.20 and 0.29 kN for the 4 mm rebars, corresponding to nominal shear strengths of 16.2 – 23.2 MPa at slips ranging from 0.63 to 1.45 mm. Specimen 3 achieved the highest response within this series, reaching 0.29 kN and 23.2 MPa at a slip of 1.38 mm. For the 10 mm rebars, higher maximum forces of 0.41 – 0.72 kN were recorded, corresponding to nominal shear strengths of 5.3 – 9.1 MPa, with Specimen 2 attaining the highest force of 0.72 kN and shear strength of 9.1 MPa at a relatively small slip of 0.65 mm. The force–slip curves in Figure 3-11 show a gradual reduction in load following the peak, with the 10 mm specimens maintaining residual load over a larger slip range. Overall, the three specimens within each diameter exhibited reasonably comparable behaviour, while the 10 mm joints carried higher absolute forces and the 4 mm joints developed higher nominal shear strengths.

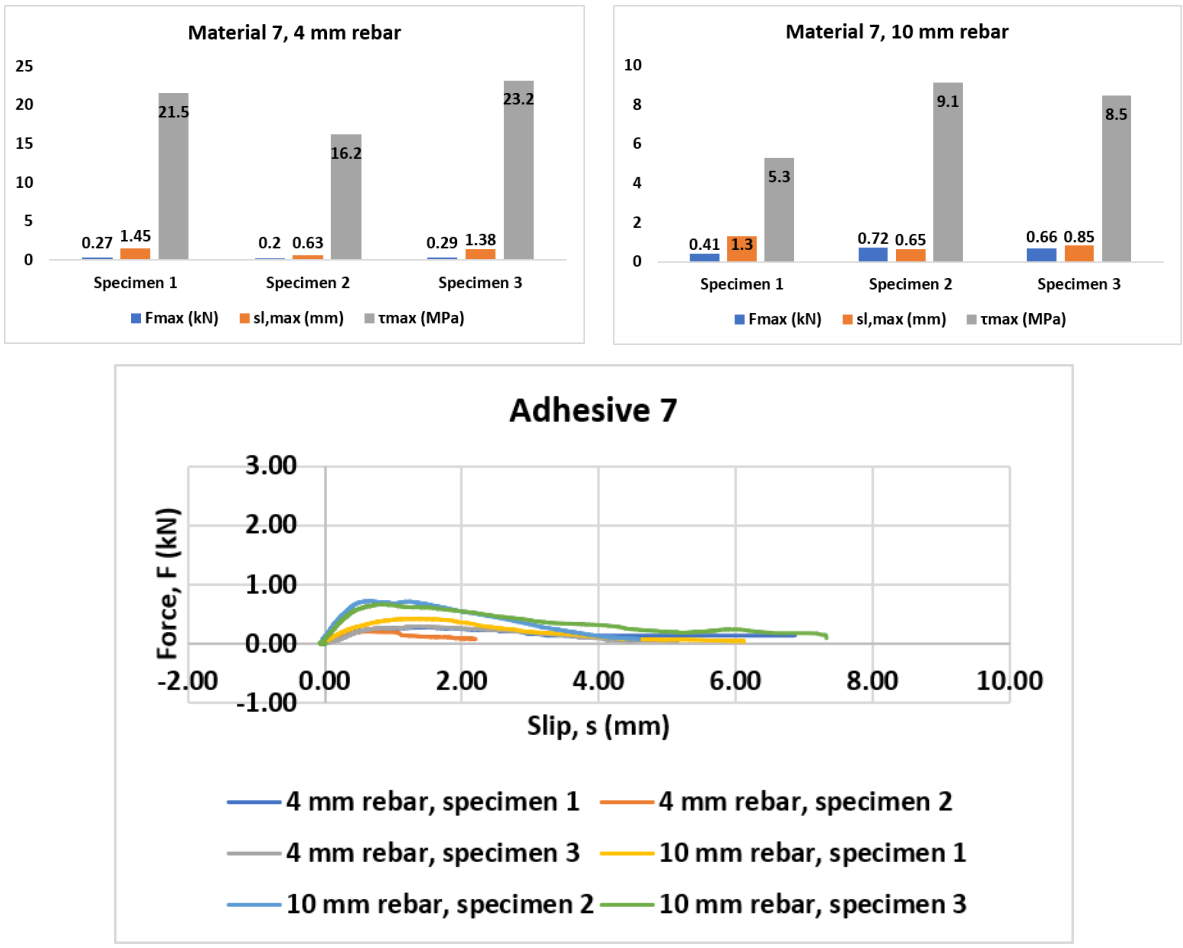


Figure 3-11 Force–slip response and joint performance of Adhesive 7 for 4 mm and 10 mm rebars.

As shown in Figure 3-12, Adhesive 8 exhibited maximum forces between 0.19 and 0.29 kN for the 4 mm rebars, corresponding to nominal shear strengths of 15.1 – 23.0 MPa at slips ranging from 0.72 to 1.11 mm, with Specimen 1 attaining the highest response of 0.29 kN and 23.0 MPa. A markedly different response was observed for the 10 mm rebars, where the maximum force ranged from 0.65 to 2.50 kN and the corresponding nominal shear strength from 8.3 to 31.8 MPa. Specimen 3 achieved the highest overall performance, reaching 2.50 kN and 31.8 MPa at a slip of 1.07 mm, followed by Specimen 1 with 2.01 kN and 25.6 MPa at 1.40 mm, whereas Specimen 2 showed considerably lower capacity. The force–slip curves in Figure 3-12 further demonstrate the pronounced response of the two higher-performing 10 mm specimens, which sustained substantial residual load over an extended slip range following the peak. Unlike the general trend observed for several preceding adhesives, Adhesive 8 enabled the 10 mm joints to develop both substantially higher absolute forces and, in two

specimens, nominal shear strengths comparable to or exceeding those obtained with the 4 mm rebars.

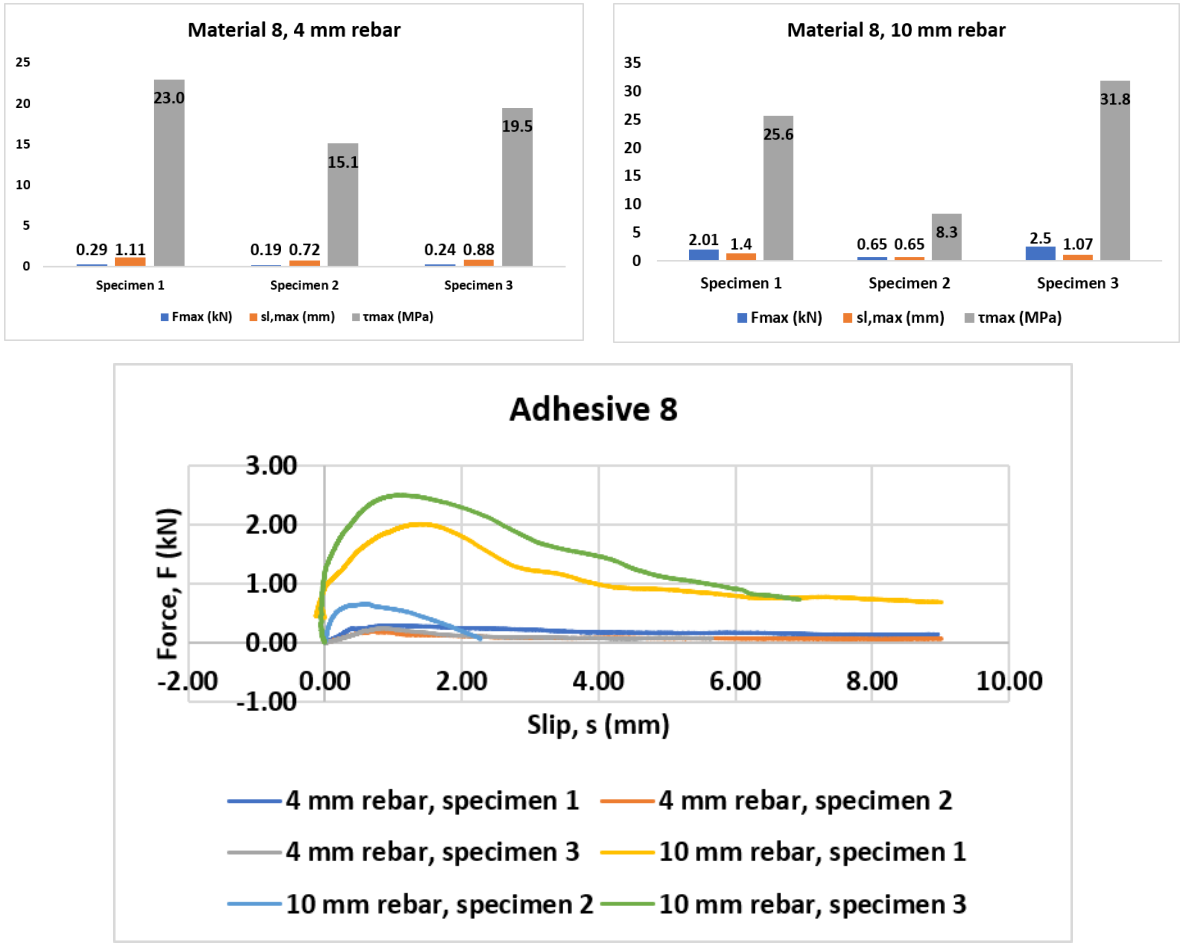


Figure 3-12 Force–slip response and joint performance of Adhesive 8 for 4 mm and 10 mm rebars.

3.3.2. Comparative Mechanical Performance

Following the assessment of the individual force–slip responses, the overall mechanical performance of the eight joining materials was compared using the mean maximum force, corresponding slip and shear strength obtained from the three specimens of each series. The coefficient of variation (CoV) was additionally considered to evaluate the consistency of the experimental response for both rebar diameters.

Table 3-4 Mean mechanical response and coefficient of variation of the tested GFRP joints.

Adhesive	Diameter (mm)	Avg. Fmax (kN)	Fmax CoV (%)	Avg. slip (mm)	slip CoV (%)	Avg. τmax (MPa)	τmax CoV (%)
Adhesive 1	4	0.2	12.8	2.7	33.0	16	11
	10	0.4	43.5	1.8	15.3	4.7	43.5
Adhesive 2	4	0.2	15.3	0.7	25.9	19.6	15.3
	10	0.6	75.0	0.7	18.6	7.8	75.5
Adhesive 3	4	0.5	30.1	1.0	17.1	39.2	30.0
	10	0.5	43.6	0.9	97.2	6.7	43.1
Adhesive 4	4	0.5	15.5	1.6	8.8	35.8	15.8
	10	1.2	43.5	1.2	43.4	15.2	43.5
Adhesive 5	4	0.3	34.5	0.8	40.2	23.6	34.1
	10	1.2	28.3	1.5	20.6	15.3	28.3
Adhesive 6	4	0.5	14.3	1.3	73.9	39.6	14.9
	10	1.6	36.0	0.8	38.6	20.2	35.9
Adhesive 7	4	0.3	18.7	1.2	39.4	20.3	18.0
	10	0.6	27.6	0.9	35.7	7.6	26.9
Adhesive 8	4	0.2	20.8	0.9	21.7	19.2	20.6
	10	1.7	55.7	1.0	36.1	21.9	55.5

The comparative results show considerable variability in the mechanical response of several test series, particularly in terms of slip and, for some configurations, maximum force. For the 4 mm rebars, the highest average nominal shear strengths were obtained with Adhesives 6 and 3, reaching 39.6 and 39.2 MPa, respectively, followed by Adhesive 4 with 35.8 MPa. In comparison, Adhesive 1 exhibited the lowest average value of 16.0 MPa. For the 10 mm rebars, Adhesive 8 provided the highest average force and nominal shear strength, reaching 1.7 kN and 21.9 MPa, respectively, followed by Adhesive 6 with 1.6 kN and 20.2 MPa. A clear diameter-dependent trend can therefore be identified: although the 10 mm joints generally sustained greater absolute forces, the 4 mm joints developed higher nominal shear strengths for all adhesives except Adhesive 8. This indicates that the increase in load capacity associated

with the larger rebar diameter was generally not proportional to the increase in the nominal cross-sectional area used for calculating shear strength.

The coefficients of variation further demonstrate that the repeatability of the joint response differed substantially between the tested configurations. Most force and shear-strength CoVs exceeded 10%, with particularly high dispersion observed for Adhesive 2 with 10 mm rebars and Adhesive 8 with 10 mm rebars. Slip exhibited even greater variability in several cases, reaching 97.2% for Adhesive 3 with 10 mm rebars and 73.9% for Adhesive 6 with 4 mm rebars. Such dispersion can be associated with the localised nature of the single-intersection joint, where relatively small variations in adhesive quantity and distribution, bond-line geometry, rebar surface condition, alignment and positioning during specimen preparation can substantially influence load transfer. The irregular surface geometry of the GFRP rebars may further contribute to differences in the effective bonded region between nominally identical specimens. Since only three specimens were tested for each configuration, an individual specimen exhibiting unusually high or low force or slip also has a pronounced influence on the calculated CoV.

3.3.3. Failure Modes and Experimental Observations

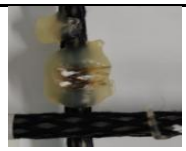
Following mechanical testing, the failed joints were visually examined to identify the dominant failure mechanisms and to relate the observed damage to the measured mechanical response. Particular attention was given to the location of failure, the condition of the adhesive after separation, damage to the GFRP surface and any differences observed between the 4 mm and 10 mm joints. Representative failure configurations are presented in the following figures, while the principal observations for each joining material are summarised and discussed.

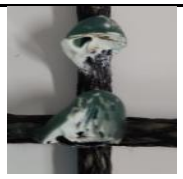
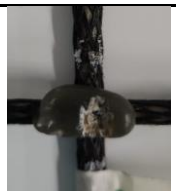
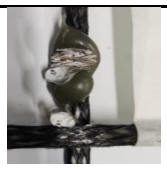
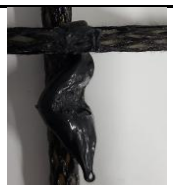
For concise identification of the observed failure mechanisms, adhesive failure at the interface adhesive/rebar and cohesive failure in the adhesive are denoted as AF and CF, respectively, in Table 3-5, while the simultaneous occurrence of both mechanisms is classified as mixed failure (MF). Particular attention was also given to variations in the surface condition and braided architecture of the GFRP rebars. The standard surface architecture consisted of six sets of braided threads arranged helically in opposing directions, corresponding to a total of 24

bobbin threads, and is designated as B24. Some rebars exhibited a denser configuration comprising 12 sets in the opposing directions, corresponding to 48 bobbin threads, and are designated as B48. Variations in the amount of surface resin were also observed, with some rebars presenting a comparatively resin-rich surface; these specimens are identified as RR. Accordingly, the codes B24, B48 and RR are used in the observation column to identify these specimen characteristics. These variations were documented because differences in braid density and surface resin condition may affect the interaction between the adhesive and the external rebar surface and may consequently contribute to variations in joint response and failure behaviour.

The failure modes and experimental observations of the 4 mm rebar joints are summarized in Table 3-5. The assessment considers the dominant failure mechanism together with relevant surface characteristics, including braid configuration and resin-rich conditions.

Table 3-5 Failure modes and experimental observations of the 4 mm GFRP rebar joints.

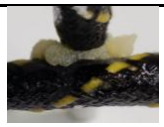
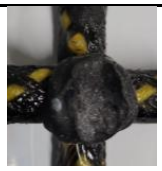
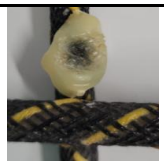
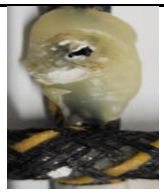
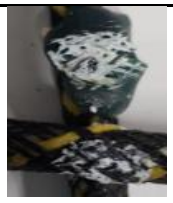
Adhesive	Specimen	Failure mode	Pictures	Main experimental observation
Adhesive 1	Specimen 1	MF (AF + CF)		B24; predominantly interfacial separation with local adhesive residue/fracture around the intersection
	Specimen 2	MF (AF + CF)		B24; interfacial debonding accompanied by visible cohesive fracture of the adhesive
	Specimen 3	AF		B24; predominantly interfacial debonding, with most adhesive remaining on one side of the joint
Adhesive 2	Specimen 1	AF		B24; predominantly interfacial debonding, with adhesive remaining mainly on the vertical rebar
	Specimen 2	MF (AF + CF)		B24; interfacial separation with local cohesive fracture of the adhesive
	Specimen 3	AF		B24; predominantly interfacial debonding, with adhesive retained mainly on one rebar
Adhesive 3	Specimen 1	CF		B24; adhesive retained on both rebars with pronounced cohesive tearing
	Specimen 2	MF (AF + CF)		B24; interfacial separation with local cohesive fracture
	Specimen 3	AF		B24; predominantly interfacial debonding, with adhesive retained mainly on one rebar
Adhesive 4	Specimen 1	MF (AF + CF)		B24; mixed interfacial separation and cohesive tearing

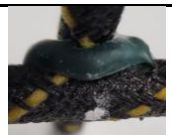
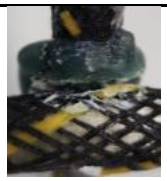
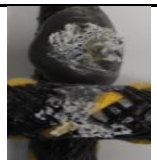
	Specimen 2	CF		B24; cohesive fracture through the adhesive layer; adhesive retained on both surfaces
	Specimen 3	CF		B24; pronounced cohesive fracture; adhesive retained on both surfaces
Adhesive 5	Specimen 1	AF		B24; predominantly interfacial debonding, with adhesive retained mainly on one rebar
	Specimen 2	AF		B24; predominantly interfacial debonding, with adhesive retained mainly on one rebar
	Specimen 3	AF		B24; predominantly interfacial debonding, with adhesive retained mainly on one rebar
Adhesive 6	Specimen 1	CF		B24; cohesive fracture through the adhesive, with adhesive retained on both surfaces
	Specimen 2	AF		B24; predominantly interfacial debonding, with the adhesive remaining largely intact on one rebar
	Specimen 3	CF		B24; clear cohesive fracture through the adhesive layer, with adhesive retained on both surfaces
Adhesive 7	Specimen 1	AF		B24; interfacial debonding with adhesive retained predominantly on one rebar
	Specimen 2	AF		B24; clear interfacial separation; adhesive retained on one rebar

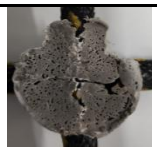
	Specimen 3	AF		B24; interfacial debonding with adhesive retained predominantly on one rebar
Adhesive 8	Specimen 1	CF		B48, RR; reduced bonding, pronounced sliding and cracking at thin section
	Specimen 2	CF		B48, RR; reduced bonding, extensive sliding/deformation and cracking at thin section
	Specimen 3	CF		B48, RR; reduced bonding, material dragging and local cracking at thin section

The corresponding failure modes and experimental observations for the 10 mm rebar joints are presented in Table 3-6. The results are examined using the same classification criteria to enable a consistent comparison of failure behaviour across the two rebar diameters.

Table 3-6 Failure modes and experimental observations of the 10 mm GFRP joints.

Adhesive	Specimen	Failure mode	Pictures	Main experimental observation
Adhesive 1	Specimen 1	AF		B48; predominantly interfacial debonding
	Specimen 2	AF		B48, RR; interfacial debonding; both rebars resin-rich
	Specimen 3	AF		B48; predominantly interfacial debonding
Adhesive 2	Specimen 1	AF		B48, RR; both rebars resin-rich; clear interfacial debonding
	Specimen 2	AF		B48, RR; one rebar resin-rich; clear interfacial debonding
	Specimen 3	AF		B48, RR; both rebars resin-rich; interfacial separation visible from top view
Adhesive 3	Specimen 1	AF		B24; interfacial debonding; adhesive retained predominantly on one rebar
	Specimen 2	AF		B24; interfacial debonding; adhesive retained predominantly on one rebar
	Specimen 3	AF		B48 & RR on one rebar; adhesive retained predominantly on one rebar
Adhesive 4	Specimen 1	AF		B24; adhesive retained predominantly on one rebar

	Specimen 2	AF		B48; top-side interfacial debonding
	Specimen 3	AF		B48 & RR on one rebar; top-side interfacial debonding
Adhesive 5	Specimen 1	CF		B24; adhesive cracking without joint separation
	Specimen 2	AF		B24; top-side interfacial debonding
	Specimen 3	AF		B24; complete interfacial separation
Adhesive 6	Specimen 1	AF		B48, RR; complete interfacial separation
	Specimen 2	AF		B48, RR; complete interfacial separation
	Specimen 3	AF		B48, RR; complete interfacial separation
Adhesive 7	Specimen 1	MF (AF + CF)		B48; predominantly interfacial separation with a small amount of adhesive retained on the opposite rebar
	Specimen 2	MF (AF + CF)		B48; predominantly interfacial separation with limited adhesive residue on both rebars

	Specimen 3	AF		B48, RR; complete interfacial debonding with adhesive retained on one rebar
Adhesive 8	Specimen 1	Sliding		B24; pronounced relative sliding without visible cracking
	Specimen 2	CF		B24; cracking through the locally reduced-thickness material zone
	Specimen 3	CF + Sliding		B24; relative sliding accompanied by cracking at the locally reduced-thickness zone

3.3.4. Overall comparison of the experimental response

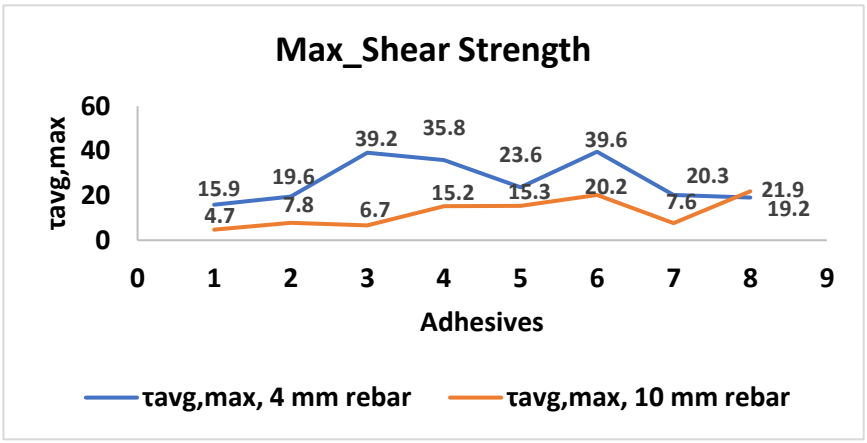


Figure 3-13 Comparison of average maximum nominal shear strength of the eight joining materials for 4 and 10 mm GFRP rebars.

As indicated in Figure 13 the overall results demonstrate a clear influence of both joining material and rebar diameter on joint performance. For the 4 mm rebars, Adhesives 6 and 3 exhibited the highest average shear strengths of 39.6 and 39.2 MPa, respectively, followed by Adhesive 4 at 35.8 MPa. For the 10 mm rebars, the highest performance was obtained with Adhesive 8, reaching an average maximum force of 1.7 kN and a shear strength of 21.9 MPa, followed by Adhesive 6 with 1.6 kN and 20.2 MPa. A consistent diameter-related trend was

observed: the 10 mm joints generally sustained greater absolute forces, whereas the 4 mm joints developed higher shear strengths, with Adhesive 8 being the main exception.



Figure 3-14 Adhesive joint geometry for (a) 4 mm and (b) 10 mm GFRP rebars.

Since Adhesive 6 exhibited the best overall experimental response, it was selected for a simplified comparison between the theoretical and experimental joint capacities. The shear strength reported in TDS for Adhesive 6 is 16.5 MPa. Based on the representative joint photographs in Figure 3-14 and using the known rebar diameters as a scale, the projected adhesive areas were estimated as approximately 62 mm² (7.2 mm x 8.6 mm) for the 4 mm joint and 269 mm² (16 mm x 16.8 mm) for the 10 mm joint. Assuming, as a first-order approximation, that the reported adhesive shear strength acts uniformly over these projected areas, the corresponding theoretical forces are approximately 1.02 kN for the 4 mm joint and 4.44 kN for the 10 mm joint.

Experimentally, however, the 4 mm specimens reached an average maximum force of approximately 0.50 kN, corresponding to a nominal shear strength of 39.6 MPa, whereas the 10 mm specimens reached approximately 1.60 kN and 20.2 MPa, respectively. Comparing the experimental force with the simplified theoretical force gives $0.5/1.02 = 49\%$ for the 4 mm joint and $1.6/4.44 = 36\%$ for the 10 mm joint. Therefore, although the 10 mm specimens carried a substantially higher absolute load (1.60 kN compared with 0.50 kN), the 4 mm specimens reached a larger fraction of the capacity estimated from their projected adhesive area.

This comparison also helps explain why the nominal shear strength calculated for the 4 mm specimens (39.6 MPa) is considerably higher than that of the 10 mm specimens (20.2 MPa). These nominal strengths were calculated by dividing the experimental maximum force by the rebar cross-sectional area, which is 12.57 mm² for the 4 mm rebar and 78.54 mm² for the 10 mm rebar. They therefore do not represent the actual shear stress acting within the adhesive

layer and should not be directly compared with the manufacturer-reported adhesive shear strength of 16.5 MPa. The 4 mm joint combines a relatively large adhesive region with a much smaller rebar cross-sectional area, resulting in a higher nominal value when the measured force is normalised by the rebar area.

The results therefore indicate that increasing the rebar diameter increases the absolute joint load capacity, as demonstrated by the increase from 0.50 kN to 1.60 kN, but does not produce a proportional increase relative to the rebar cross-sectional area. In the present specimens, the smaller 4 mm joints appear to utilise the available adhesive region more effectively, reaching approximately 49% of the simplified theoretical estimate compared with 36% for the 10 mm joints. Nevertheless, the larger radius of the 10 mm rebar provides a locally flatter contact geometry, which could be favourable for bonding. Consequently, the observed diameter effect cannot be attributed to cross-sectional area alone, but appears to depend on the relationship between rebar geometry, adhesive distribution and the effective load-transfer region.

Considerable variability was observed between nominally identical specimens, particularly in the 10 mm series and in the measured slip. Force and shear strength CoVs frequently exceeded 10%, reaching approximately 75% for Adhesive 2 with 10 mm rebars, while slip CoV reached 97.2% for Adhesive 3 with 10 mm rebars and 73.9% for Adhesive 6 with 4 mm rebars. The greater dispersion in slip indicates that the displacement required to reach maximum force was generally less repeatable than the load capacity itself. This variability can be related to the highly localised nature of the bonded intersection and to differences observed in the GFRP surface condition. In particular, B24 and B48 braid configurations were encountered together with resin-rich surfaces. The denser B48 architecture and resin-rich regions altered the external surface available for bonding and may have affected adhesive interaction and mechanical interlocking. Variations in adhesive quantity, bond-line geometry and effective contact area may have further contributed to the observed scatter. Since these parameters were not independently controlled, however, their individual influence cannot be quantitatively isolated from the present results.

The failure observations reinforce the importance of the adhesive–GFRP interface. Several specimens exhibited adhesive failure, characterised by interfacial debonding and retention of the joining material predominantly on one rebar, while others developed cohesive or mixed failure. The occurrence of different failure mechanisms among nominally identical specimens helps explain some of the observed variation in force and slip. Adhesive 8 exhibited a particularly distinct response, with pronounced relative sliding and deformation of the thermoplastic material rather than the conventional debonding behaviour observed for most other joining systems. Cracking was also observed through locally reduced-thickness regions produced by the mould geometry. Interestingly, its 4 mm specimens were associated with B48 and resin-rich surfaces and showed comparatively modest performance, whereas the B24 10 mm specimens achieved the highest average response of the 10 mm series. This further suggests that joint performance depended strongly on the interaction between the joining material, rebar surface and local joint geometry.

Overall, the results show that the selection of a joining material cannot be based solely on its nominal material properties or on maximum joint strength. Adhesive 6 demonstrated particularly strong performance across both rebar diameters, while other materials showed substantial changes in ranking between the 4 and 10 mm configurations. Strength, repeatability, failure mechanism and compatibility with the actual GFRP surface must therefore be considered together. The relatively high experimental dispersion also highlights an important requirement for future automated mesh production: controlling the rebar surface condition, braid configuration, joining-material quantity and intersection geometry will be essential for achieving repeatable joint performance.

3.4. Summary

This chapter presented the materials, experimental methodology and mechanical assessment of the proposed GFRP rebar joints using eight different joining materials and two rebar diameters. The experimental results demonstrated that joint performance was governed not only by the joining material but also by rebar diameter, surface architecture and local bonding conditions. Considerable differences were observed in load capacity, nominal shear strength, slip, repeatability and failure behaviour, with variations in braid configuration and resin-rich surfaces identified as relevant characteristics affecting the bonded interface. The findings provide the experimental basis for evaluating the suitability of the investigated joining systems and for the subsequent development of a reliable and repeatable joining approach for GFRP mesh production.

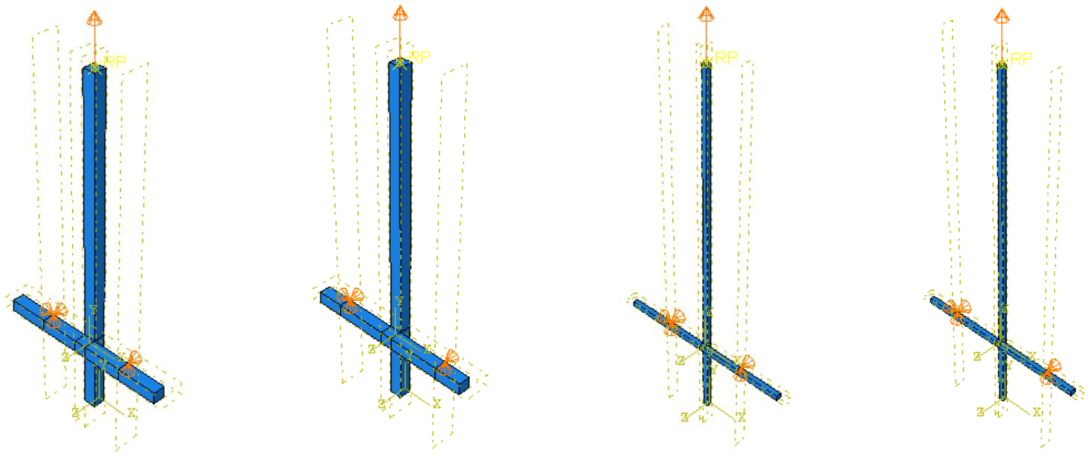
THIS PAGE WAS INTENTIONALLY LEFT BLANK

4. NUMERICAL MODELLING OF GFRP REBAR JOINTS

An Implicit numerical model was developed in Abaqus to investigate the mechanical response of a single GFRP grid intersection and to complement the experimental investigation presented in the previous chapter. The model reproduced the one-joint configuration subjected to tensile loading, with the interaction between the intersecting rebars represented using a surface-based cohesive modelling approach. The cohesive behaviour was defined through damage initiation and evolution parameters representative of commonly adopted epoxy-based cohesive systems, based on established numerical modelling guidance. Appropriate geometrical simplifications were introduced to obtain a computationally efficient representation while preserving the principal load-transfer mechanism of the joint. In addition to evaluating the force–displacement response of the connection, the numerical model was used to investigate the influence of the clamping distance along the horizontal rebar, allowing the effect of the support position on the predicted joint response to be assessed. The numerical results were subsequently compared with the experimental behaviour to evaluate the ability of the model to reproduce the mechanical response observed during tensile testing.

4.1. Cohesive Zone Modelling Approach

A three-dimensional numerical model of a single GFRP grid intersection was developed in Abaqus using a surface-based cohesive zone modelling (CZM) approach. The model consisted of two orthogonally positioned rebars with nominal diameters of 4 and 10 mm, representing the configuration adopted in the experimental programme. To obtain a well-defined and constant cohesive interaction area at the intersection, the circular rebar cross-section was idealised as an equivalent square section while maintaining the same cross-sectional area. This resulted in square dimensions of approximately 3.54 mm × 3.54 mm and 8.86 mm × 8.86 mm for the 4 and 10 mm rebars, respectively. The numerical study additionally considered two clamping distances, 30 and 40 mm from the joint region along the horizontal rebar, to evaluate the influence of the restraint position on the predicted joint response. The adopted geometry and loading arrangement are illustrated in Figure 4-1.



(a) (b) (c) (d)

Figure 4-1 Geometry of 10 mm and 4 mm rebars clamped at (a) 30 mm, (b) 40 mm, (c) 30 mm & (d) 40 mm from joint

The GFRP rebars were represented using orthotropic elastic behaviour. The longitudinal elastic modulus (E1) was taken as 50 GPa based on the manufacturer-provided value, whereas the remaining elastic constants were assumed to complete the orthotropic material definition required for the numerical model.

Table 4-1 GFRP rebars mechanical properties

Property	Value
E1	50 GPa
E2	12.5 GPa
E3	12.5 GPa
Nu12	0.3
Nu13	0.3
Nu23	0.35
G12	5.25 GPa
G13	5.25 GPa
G23	3.48 GPa

The interaction between the two rebars was represented using surface-based cohesive behaviour. An uncoupled traction–separation formulation was adopted, with independently defined normal and shear stiffnesses. Damage initiation was governed by a quadratic nominal traction criterion, while subsequent degradation was described using linear, energy-based damage evolution. Since adhesive-specific cohesive properties were not experimentally characterised, the cohesive and damage parameters were adopted as representative values

for commonly modelled epoxy systems [23]. A small viscosity coefficient was included for numerical stabilisation, while hard contact in the normal direction allowed separation following loss of cohesive interaction. Table 4-2 includes the cohesive and damage parameters adopted for the joint interface simulation.

Table 4-2 Cohesive and damage parameters adopted for the joint interface.

Parameter	Adopted value
Normal stiffness, K_{nn}	8000 N/mm³
Shear stiffness, $K_{ss} = K_{tt}$	2860 N/mm³
Damage initiation	Quadratic traction
Normal nominal strength	20 MPa
Shear nominal strength, directions 1 and 2	20 MPa
Damage evolution	Energy-based, linear
Fracture energy	2.06 N/mm
Viscosity coefficient	1×10−5
Normal contact	Hard contact; separation allowed

The boundary conditions were selected to reproduce the restraint and tensile-loading concept of the experimental test. The horizontal rebar was restrained at the prescribed clamping locations using a simply supported representation. At one clamping region, translational degrees of freedom were restrained ($U_1 = U_2 = U_3 = 0$), while at the opposite region the transverse translations U_2 and U_3 were constrained, allowing the longitudinal degree of freedom required to avoid unnecessary over-constraint of the horizontal member. Two clamping positions, located 30 and 40 mm from the joint region, were investigated. Tensile loading was introduced through displacement control at the upper end of the vertical rebar, where a displacement of 5 mm was prescribed in the loading direction (U_2), while the remaining translational and rotational degrees of freedom were constrained. This arrangement allowed the vertical member to be pulled relative to the restrained horizontal rebar while maintaining the intended joint configuration.

Finally, the models were discretised using global mesh sizes proportional to the respective rebar dimensions. A global element size of 1.775 mm was adopted for the 4 mm model and 4.43 mm for the 10 mm model. The same modelling procedure, interaction definition and

loading approach were maintained across the investigated configurations to enable direct assessment of the effects of rebar diameter and clamping distance.



(a) (b)

Figure 4-2 Global mesh size of 10 mm rebar (a) 4.43 mm & 4 mm rebar (b) 1.775 mm

4.2. Numerical Results and Experimental Comparison

The influence of the horizontal rebar clamping distance on the numerical response is presented in Figure 4-3 for both rebar diameters. For the 4 mm rebar, maximum forces of 0.22 and 0.20 kN were obtained for clamping distances of 30 and 40 mm, respectively, indicating only a minor reduction in load capacity with increasing distance from the joint. A similar trend was obtained for the 10 mm rebar, for which the maximum force decreased from 1.37 kN at a clamping distance of 30 mm to 1.31 kN at 40 mm. Although the difference in peak force was relatively small for both diameters, the force–slip curves show that the clamping distance influenced the deformation response of the assembly. The 40 mm configuration allowed a larger slip before reaching the maximum force, particularly for the 4 mm rebar, whereas the 30 mm configuration produced a comparatively stiffer response. This behaviour can be attributed to the greater unsupported length of the horizontal rebar at the larger clamping distance, which increases the flexibility of the assembly. Overall, the 30 mm clamping distance produced slightly higher maximum forces for both diameters and was therefore selected for the subsequent comparison with the experimental response.

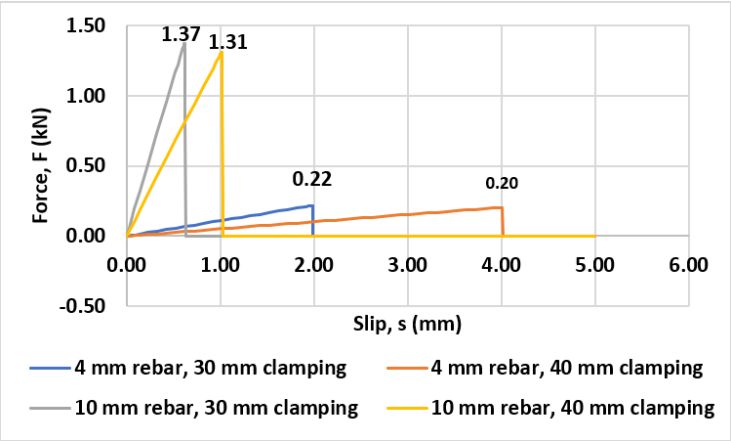


Figure 4-3 Influence of clamping distance on the numerical force–slip response of the 4 mm and 10 mm GFRP joints.

For comparison with the numerical model, representative experimental specimens were selected from Chapter 3 based on their maximum nominal shear stresses being close to the 20 MPa cohesive strength prescribed in the numerical model. For the 4 mm rebar, Adhesive 8 – Specimen 3 was selected, which developed a maximum nominal shear stress of 19.47 MPa. For the 10 mm rebar, Adhesive 6 – Specimen 1 was selected, with a corresponding maximum nominal shear stress of 19.13 MPa. This selection provided experimental cases with interface strength levels comparable to the 20 MPa nominal traction adopted for damage initiation in the CZM model, rather than selecting specimens solely on the basis of their maximum force.

Since Abaqus directly provided the displacement of the loaded rebar, the numerical displacement was converted to slip following the same procedure adopted for the experimental results. The elastic elongation of the GFRP rebar was removed according to Fl/EA, using $E = 50$ GPa and the corresponding cross-sectional area for each rebar diameter. As no physical extensometer gauge length exists in the numerical model, $L = 25$ mm was retained to maintain consistency with the experimental slip calculation. The resulting numerical and experimental force–slip responses are compared in Figure 4-4.

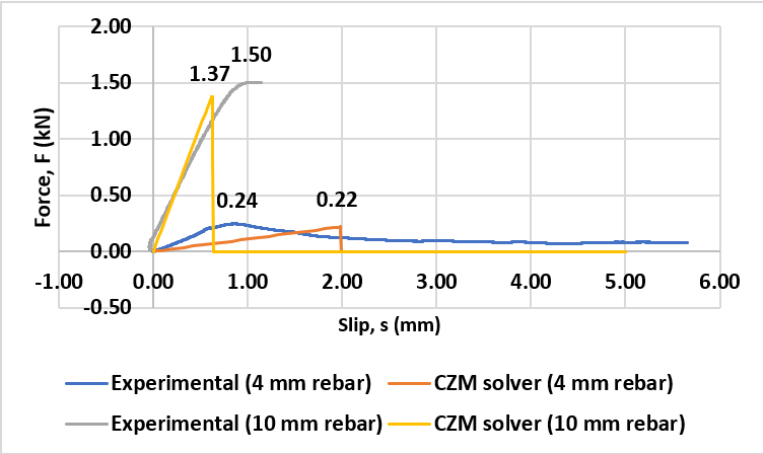


Figure 4-4 Comparison of experimental and numerical force–slip responses for the 4 mm and 10 mm GFRP joints at a 30 mm clamping distance.

The comparison shows good agreement in terms of maximum load, particularly considering the simplified geometry and generic cohesive parameters adopted in the numerical model. For the 4 mm joint, the experimental specimen reached approximately 0.24 kN, compared with 0.22 kN predicted by the CZM model, corresponding to an underprediction of approximately 8.3%. For the 10 mm joint, the experimental maximum force was approximately 1.50 kN, while the numerical model predicted 1.37 kN, giving an underprediction of approximately 8.7%. The similarity in peak capacity for both diameters indicates that the adopted cohesive formulation can reasonably reproduce the load level associated with joint failure when an experimental specimen of comparable nominal shear strength is considered.

Greater differences are evident in the deformation and post-peak responses. For the 4 mm rebar, the experimental curve reaches its maximum force at a smaller slip and subsequently exhibits a gradual reduction in load, whereas the numerical model continues approximately linearly to a larger slip before a sudden loss of load-carrying capacity. For the 10 mm rebar, both responses are comparatively stiff, although the numerical model again predicts a sharper failure once the damage criterion is reached. These differences are expected because the CZM model represents an idealised interface with uniform cohesive properties and prescribed linear damage evolution, whereas the experimental joints contain irregular adhesive geometry, braided GFRP surfaces, local resin variations and progressive interfacial damage.

The numerical model therefore reproduces the peak capacity more closely than the complete evolution of the experimental force–slip response.

4.3. Summary

The numerical investigation demonstrated that the proposed surface-based CZM approach could reasonably reproduce the maximum load capacity of the experimentally tested GFRP joints, with differences of less than 10% for both rebar diameters considered. The clamping-distance study showed a slightly higher joint capacity and stiffer response for the 30 mm configuration compared with 40 mm. Greater differences were observed in the deformation and post-peak behaviour, reflecting the idealised geometry and cohesive properties adopted in the numerical model compared with the variability of the experimental joints. Overall, the model provides a simplified numerical representation of the joint response and demonstrates the applicability of the CZM approach for investigating GFRP grid intersections.

THIS PAGE WAS INTENTIONALLY LEFT BLANK

5. CONCLUSIONS AND FUTURE WORK

5.1. Key Findings

This dissertation investigated the feasibility and mechanical behaviour of localised joining techniques for the production of braided GFRP rebar grids. The work was motivated by the need for a joining solution capable of forming individual grid intersections while remaining compatible with the characteristics of composite reinforcement and, ultimately, with an automated manufacturing process. The literature review showed that FRP grids have already demonstrated considerable potential in civil infrastructure, strengthening and lightweight structural applications. However, most existing grid systems rely on embedded, mechanically assembled or externally bonded configurations, while the available welding literature is largely focused on flat composite laminates. Consequently, the localised joining of intersecting, curved thermoset GFRP rebars remains comparatively unexplored.

The experimental programme therefore evaluated eight joining materials across two braided GFRP rebar diameters, 4 and 10 mm, using 48 single-intersection specimens. The results demonstrated that joint behaviour cannot be attributed to the joining material alone. Rebar diameter, surface architecture, local resin condition, adhesive distribution and effective joint geometry all contributed to the measured response. The 10 mm joints generally carried greater absolute forces, whereas the 4 mm joints developed higher nominal shear strengths. This difference should not be attributed solely to the change in rebar cross-sectional area, as the adhesive–rebar contact geometry also varies with diameter. The experimental and simplified theoretical comparison indicated that the 4 mm joints utilised a greater proportion of the estimated adhesive region relative to their nominal rebar area, while the larger radius of the 10 mm rebars provided a locally flatter contact geometry. Consequently, the effect of rebar diameter appears to depend on the combined influence of rebar geometry, adhesive distribution and the effective load-transfer region.

Among the investigated materials, Adhesives 3 and 6 provided the highest average shear strengths for the 4 mm rebars, reaching 39.2 and 39.6 MPa, respectively. For the 10 mm rebars, the highest average values were obtained with Adhesives 8 and 6, reaching 21.9 and 20.2 MPa, respectively. Adhesive 6 therefore showed particularly promising performance because it remained among the strongest systems for both diameters. Adhesive 8 exhibited a different response from the thermosetting adhesives. Rather than conventional interfacial debonding, pronounced material deformation, sliding and local cracking were observed, demonstrating the potential of a thermoplastic joining concept while also revealing the importance of controlling material thickness and joint geometry.

A major outcome of the experimental investigation was the substantial variability observed between nominally identical specimens. Examination of the failed joints provided an explanation for at least part of this dispersion. The braided rebars did not present completely uniform surfaces: B24 and B48 braid configurations were encountered together with resin-rich regions. These variations changed the surface available for bonding and potentially the degree of mechanical interlocking between the adhesive and the rebar. Variations in deposited material, bond-line geometry and local contact conditions further influenced the failure response. Adhesive, cohesive and mixed failure mechanisms were consequently observed, sometimes within the same test series. These findings demonstrate that achieving high strength alone is insufficient for developing a reliable grid-production process; repeatability and control of the rebar surface and joining operation are equally important.

The numerical investigation provided an additional assessment of the single-joint response using a surface-based cohesive zone model. The model also enabled the influence of horizontal-rebar clamping distance to be studied independently. Increasing the clamping distance from 30 to 40 mm slightly reduced the predicted maximum force and increased the flexibility of the assembly for both rebar diameters. The 30 mm configuration was therefore used for comparison with representative experimental specimens having nominal shear strengths close to the 20 MPa cohesive strength adopted numerically. Maximum forces of 0.22 and 1.37 kN were predicted for the 4 and 10 mm models, compared with approximately 0.24 and 1.50 kN experimentally, corresponding to differences below 10%. The model therefore reproduced the peak load reasonably well despite the geometrical simplifications

and use of generic cohesive parameters. Greater differences occurred in the slip and post-peak response because the numerical interface was idealised, whereas the physical joints exhibited irregular material distribution, braided surfaces and progressive damage.

Taken together, the experimental and numerical results demonstrate that localised bonding is a feasible approach for manufacturing GFRP grid intersections, but they also identify manufacturing consistency as the principal challenge. The results do not support the selection of a joining material based solely on manufacturer properties or the highest measured strength. A suitable system must combine sufficient load-transfer capacity with repeatable deposition, compatibility with the braided GFRP surface, controlled failure behaviour, practical processing time and suitability for automation. Within the investigated materials, Adhesive 6 provided the most consistently strong mechanical response across the two rebar diameters, while the thermoplastic concept represented by Adhesive 8 remains particularly interesting from a manufacturing perspective because of its rapid heat-activated joining mechanism and absence of a conventional curing period.

Overall, this work establishes an experimental and numerical basis for the development of locally bonded braided GFRP grids. More importantly, it shows that future improvement should not focus exclusively on increasing adhesive strength. Controlling the complete joint system from rebar surface architecture and material deposition to joint geometry and processing conditions is necessary to obtain a reliable and scalable grid-manufacturing process.

5.2. Future Work

The present investigation also identifies several areas requiring further development before the proposed joining concept can be transferred to automated production. The most immediate priority is to reduce the experimental variability by controlling the B24/B48 braid configuration, resin-rich surface regions, adhesive quantity and joint dimensions. Future testing should use rebars with systematically characterised surfaces and a controlled material-deposition procedure so that the influence of each parameter can be isolated. Increasing the number of specimens per configuration would also provide a stronger statistical basis for assessing repeatability.

Based on the present mechanical results, further optimisation could concentrate on Adhesive 6 as a strong thermosetting candidate and Adhesive 8 as a rapid thermoplastic alternative. For the latter, particular attention should be given to mould design and uniform material thickness, since cracking was associated with locally reduced material regions. Processing parameters such as deposited volume, heating temperature, pressure, cooling time and joint dimensions should be systematically optimised. The feasibility of automated dispensing or localised heating should subsequently be investigated to determine whether consistent intersections can be produced at the cycle times required for mesh manufacture.

Although the experimental programme focused on chemical/adhesive-based localised joining, future work should broaden the investigation to other joining techniques identified in the literature review. In particular, resistance, ultrasonic and infrared-based approaches, including the use of suitable thermoplastic interlayers or local energy directors, should be assessed experimentally for braided GFRP rebar intersections. Comparing these routes under a common test configuration would help determine whether they can provide shorter cycle times, improved repeatability and greater compatibility with automated grid production.

The numerical model should also be refined using experimentally characterised cohesive properties rather than generic epoxy parameters. The present equivalent-square representation could be replaced by the actual circular/braided geometry, and adhesive thickness, surface irregularities and progressive mixed-mode damage could be incorporated. A mesh-sensitivity study and calibration against a larger set of experimental curves would allow the model to move from qualitative assessment towards predictive optimisation of joint geometry and processing parameters.

Finally, the investigation should progress from isolated intersections towards complete GFRP grid assemblies. Grid-level testing would establish how local joint behaviour influences global load distribution and whether failure of one intersection redistributes forces to neighbouring joints. Long-term durability under moisture, temperature, alkaline exposure, cyclic loading and ageing should also be evaluated for the most promising joining systems. These steps would provide the connection between the single-joint feasibility demonstrated in this dissertation and the development of a repeatable, durable and automated manufacturing process for braided GFRP reinforcement grids.

REFERENCES

[1] R. H. L. Chen, J.-H. Choi, H. V. GangaRao, and P. A. Kopac, “Steel Versus GFRP Rebars?,” *Public Roads*, vol. 72, no. 2, 2008, [Online]. Available: https://www.fhwa.dot.gov/publications/publicroads/08sep/01.cfm

[2] J. Liao *et al.*, “Behavior of FRP grid-reinforced ultra-high performance concrete (UHPC) pipes under lateral compression,” *Case Studies in Construction Materials*, vol. 19, p. e02189, Dec. 2023, doi: 10.1016/j.cscm.2023.e02189.

[3] S. Gao *et al.*, “Experimental investigation on reinforced concrete with corroded stirrups strengthened by CFRP grid and GFRP jacket,” *Mater Struct*, vol. 59, no. 3, p. 147, Apr. 2026, doi: 10.1617/s11527-026-03032-5.

[4] P. Liu *et al.*, “Axial compressive behavior of concrete columns strengthened with BFRP grids,” *Construction and Building Materials*, vol. 477, p. 141305, May 2025, doi: 10.1016/j.conbuildmat.2025.141305.

[5] P. Christou, A. Michael, C. Anastasiou, and D. Nicolaides, “Effect of confinement on the interaction diagrams for rc sections with cfrp grids and wraps,” *Int. J. CMEM*, vol. 1, no. 3, pp. 265–282, May 2013, doi: 10.2495/CMEM-V1-N3-265-282.

[6] D. Lu *et al.*, “Seismic design of FRP grid and bar strengthened RC columns via multi-objective optimization and decision analysis,” *Construction and Building Materials*, vol. 519, p. 145826, Apr. 2026, doi: 10.1016/j.conbuildmat.2026.145826.

[7] L. Pavlov, I. te Kloeze, B. J. R. Smeets, and S. M. Simonian, “Development of Mass and Cost Efficient Grid-Stiffened and Lattice Structures for Space Applications,” presented at the 16th European Conference on Spacecraft Structures, Materials and Environmental Testing, Toulouse, France, 2016.

[8] C. Schmidt and J. Hegger, “Experimental investigations on bond behaviour and crack development in concrete members reinforced with carbon textile grids subjected to cyclic loading,” *Construction and Building Materials*, vol. 466, p. 140168, Mar. 2025, doi: 10.1016/j.conbuildmat.2025.140168.

[9] R. Guo, Y. Pan, L. Cai, and S. Hino, “Bonding behavior of CFRP grid-concrete with PCM shotcrete,” *Engineering Structures*, vol. 168, pp. 333–345, Aug. 2018, doi: 10.1016/j.engstruct.2018.04.059.

[10] A. Di Tommaso, C. Gentilini, and G. Castellazzi, *Mechanics of Masonry Structures Strengthened with Composite Materials II: MuRiCo5*, vol. 747. Trans Tech Publications Ltd, 2017. doi: 10.4028/b-lYG0Rn.

[11] L. An, X. Li, C. Jin, W. Zhao, and Q. Shi, “An extrinsic welding method for thermosetting composites: Strong and repeatable,” *Composites Part B: Engineering*, vol. 245, p. 110224, Oct. 2022, doi: 10.1016/j.compositesb.2022.110224.

[12] F. M. De Oliveira Campos, T. B. Da Costa, R. M. Di Benedetto, L. C. M. Barbosa, and A. C. Ancelotti Junior, “Infrared Welding as an Efficient Joining Method for Sustainable Thermoplastic Composites,” *Appl Compos Mater*, vol. 33, no. 2, p. 66, Apr. 2026, doi: 10.1007/s10443-025-10436-z.

[13] K. Stankiewicz, A. Lipkowski, P. Kowalczyk, M. Giżyński, and B. Waśniewski, “Resistance Welding of Thermoplastic Composites, Including Welding to Thermosets and Metals: A Review,” *Materials*, vol. 17, no. 19, p. 4797, Sep. 2024, doi: 10.3390/ma17194797.

[14] T. Maierhofer, E. G. Loukaides, C. Carr, C. Bisagni, and R. Butler, “Resistance-welded thermoset composites: A Bayesian approach to process optimisation for improved

fracture toughness," *Composites Part A: Applied Science and Manufacturing*, vol. 177, p. 107894, Feb. 2024, doi: 10.1016/j.compositesa.2023.107894.

[15] A. Meram, "Technical Challenges and Limitations in Ultrasonic Welding of Thermoplastic Composites," in *7th International Congress on Engineering and Sciences*, Istanbul, Türkiye, Sep. 2025.

[16] Y. Li, Z. Liu, W. Liao, Y. Li, L. Deng, and Y. Zhang, "High-Quality Spot and Continuous Ultrasonic Welding of Carbon Fiber Reinforced Polyetheretherketone (CF/PEEK) Composites Using PEEK Mesh Energy Directors," *Appl Compos Mater*, vol. 33, no. 1, p. 46, Feb. 2026, doi: 10.1007/s10443-025-10419-0.

[17] D. Yue, G. Zhao, J. Pan, J. Liu, and D. Quan, "Ultrasonic welding of thermoplastic composites with woven mesh energy directors: Enhanced strength and hygrothermal resistance," *Journal of Materials Research and Technology*, vol. 36, pp. 9699–9712, May 2025, doi: 10.1016/j.jmrt.2025.05.137.

[18] F. Yao, Z. Li, Y. Zhao, Y. Wei, T. Yan, and X. Cao, "Enhancing process stability in continuous ultrasonic welding of CFRTP: A welding speed-quality uniformity correlation study," *Int J Adv Manuf Technol*, vol. 142, no. 1–2, pp. 949–962, Jan. 2026, doi: 10.1007/s00170-025-17058-6.

[19] A. Thailand, "EWT 150 Series Multi-Resin Compatible Roving (Direct Roving)," ACM Thailand, Technical Data Sheet.

[20] Westlake Epoxy, "EPIKOTE Resin TRAC 06110 + EPIKURE Curing Agent 06739," Westlake Epoxy, Technical Data Sheet, Jun. 2025.

[21] The Light Rebar Company, "Braided Composite Rebar," The Light Rebar Company, Technical Data Sheet.

[22] British Standards Institution, "Steel for the reinforcement and prestressing of concrete - Test methods - Part 2: Welded fabric," British Standards Institution, 2002.

[23] Ata Khabaz, *Mastering CZM Damage Simulation in ABAQUS: Step-by-Step Tutorial for Adhesive Joints*, (Aug. 28, 2023). [Youtube Video]. Available: https://www.youtube.com/watch?v=5IjW1DxePRg